STRESS AND FRACTURE ANALYSES UNDER ELASTIC-PLASTIC AND CREEP CONDITIONS: SOME BASIC DEVELOPMENTS AND COMPUTATIONAL APPROACHES*

K. W. Reed, R. B. Stonesifer,** and S. N. Atluri
Georgia Institute of Technology
Atlanta, Georgia 30032

Abstract:

In Part I of this paper a new hybrid-stress finite element algorithm, suitable for analyses of large quasi-static deformations of inelastic solids, is presented. Principal variables in the formulation are the nominal stress-rate and spin. As such, a consistent reformulation of the constitutive equation is necessary, and is discussed. The finite element equations give rise to an initial value problem. Time integration has been accomplished by Euler and Runge-Kutta schemes and the superior accuracy of the higher order schemes is noted. In the course of integration of stress in time, it has been demonstrated that classical schemes such as Euler's and Runge-Kutta may lead to strong frame-dependence. As a remedy, modified integration schemes are proposed and the potential of the new schemes for suppressing frame dependence of numerically integrated stress is demonstrated. The applicability of explicit and implicit forward gradient schemes to improve the stability of time-integration in large deformation problems is investigated. The feasibility and performance of the present methods are demonstrated in a number of problems, and it is found that the stresses obtained by the present method are of exceptional accuracy, much more than could be expected of an assumed-velocity based finite element algorithm.

In Part II of this paper, the topic of the development of valid creep fracture criteria is addressed. Until now, the so-called C* integral, intro-

---

*A report of research supported under NASA Grant NAG 3-38.

**Formerly a Doctoral Candidate (now graduated and in private eng. practice).

duced by Goldman and Hutchinson, was attempted to be used in the literature to correlate creep crack growth rate. In the present work, a new path-independent integral parameter $(\dot{\underline{T}})$ which has a considerably more degree of generality and validity than the C* integral, is introduced. The mathematical aspects of this parameter are first reviewed by deriving generalized vector forms of the parameters $(\dot{\underline{T}})$ and $\underline{C}^*$; using conservation laws which are valid for arbitrary, three-dimensional cracked bodies with (macro)-crack surface tractions, body forces, inertial effects and large deformations. Two principal conclusions are that $(\dot{\underline{T}})$ is a valid crack-tip parameter during nonsteady as well as steady-state creep and that $(\dot{\underline{T}})$ has an energy rate interpretation whereas $\underline{C}^*$ does not. Using this new integral, and a finite element analysis procedure, several fundamental aspects of creep crack-growth are studied numerically. Specifically numerical results are presented for a double-edge-crack specimen for which experimental results are available. Finally, a simplified methodology for predicting creep growth behaviour is presented, based on the conclusions drawn from the present numerical simulations of experimental data.

Part I: Stress Analysis of Inelastic Solids Using Assumed Stress Finite Elements

Nomenclature:

$C(\tau)$ configuration (image of the body in space at time τ)

$\underline{X}$ position vector in space at time τ

$\underline{x}$ position vector in space at (present) time t

$\nabla = \underline{e}^i\,\partial/\partial x^i$; $\nabla_X = \underline{e}^I\,\partial/\partial X^I$; $\dot{a} = \partial a/\partial t + \underline{V}.\nabla a$ material derivative of 'a'

$\underline{\chi}_\tau$ deformation function; maps $C(\tau)$ to $C(t)$ as

$$\underline{x} = \underline{\chi}_\tau(\underline{X},t)$$

$\underline{V}$ velocity function; related to deformation function as

$$\underline{V}(\underline{\chi}_\tau(\underline{X},t),t) = \dot{\underline{\chi}}_\tau(\underline{X},t)$$

$\underset{\sim}{F}_\tau \equiv (\nabla_X \underline{X}_\tau(\underline{X},t))^T$ deformation gradient

$J_\tau = \det \underset{\sim}{F}_\tau$

$\underset{\sim}{L} = (\nabla \underline{V}(\underline{x},t))^T$ velocity gradient

$\dot{J} = \nabla . \underline{V}(\underline{x},t)$ dilitation

$\underset{\sim}{\varepsilon} = \frac{1}{2}(\underset{\sim}{L}+\underset{\sim}{L}^T)$ stretching

$\underset{\sim}{\omega} = \frac{1}{2}(\underset{\sim}{L}-\underset{\sim}{L}^T)$ spin

$\underline{T}$ true traction; $\underline{T}_\tau$ nominal traction relative to $C(\tau)$

$\underset{\sim}{\tau}$ true stress; $\underset{\sim}{\sigma}_\tau = J_\tau \underset{\sim}{\tau}$ Kirchhoff stress relative to $C(\tau)$

$\underset{\sim}{t}_\tau = \underset{\sim}{F}_\tau^{-1} \underset{\sim}{\sigma}_\tau$ nominal stress relative to $C(\tau)$

$\dot{\underline{T}}$ true traction rate; $\dot{\underline{T}}_\tau$ nominal traction rate

$\dot{\underset{\sim}{\sigma}} = \dot{J}\underset{\sim}{\tau} + \dot{\underset{\sim}{\tau}}$ Kirchhoff stress rate

$\dot{\underset{\sim}{t}} = -(\underset{\sim}{\varepsilon}+\underset{\sim}{\omega}) . \underset{\sim}{\tau} + \dot{\underset{\sim}{\sigma}}$ nominal stress rate

$\dot{\underset{\sim}{\sigma}}{}^* = \dot{\underset{\sim}{\sigma}} - \underset{\sim}{\omega} . \underset{\sim}{\tau} + \underset{\sim}{\tau} . \underset{\sim}{\omega}$ 'corotational' stress rate

Introduction:

The research which produced the present hybrid stress fintie element algorithm was motivated by the observation that hybrid stress algorithms consistently outperform those using velocity (or displacement) as the sole variable. Hybrid stress models for infinitesimal deformation of shells and incompressible solids have been topics of intense research since Pian's first presentation of such a model in [1]. However, hybrid stress models for finite deformations have only been researched since de Veubeke's [2] presentation of a complementary energy principle for finite elastic deformations, and Atluri's [3], [4] generalization of that principle for inelastic solids. A hybrid stress model for finite elastic deformation was presented by Murakawa [5]. In this report a hybrid stress model for finite inelastic deformation is detailed.

The Boundary Value Problem:

Compatibility

$$\nabla X(\underset{\sim}{\varepsilon}-\underset{\sim}{\omega}) = 0; \qquad (I.1)$$

Linear Momentum Balance (LMB)

$$\nabla\cdot\dot{\underset{\sim}{t}} + \rho\dot{\underline{b}} = \underline{0}; \qquad (I.2)$$

Angular Momentum Balance (AMB)

$$[(\underset{\sim}{\varepsilon}+\underset{\sim}{\omega})\cdot\underset{\sim}{\tau}+\dot{\underset{\sim}{t}}] - [(\underset{\sim}{\varepsilon}+\underset{\sim}{\omega})\cdot\underset{\sim}{\tau}+\dot{\underset{\sim}{t}}]^T = \underset{\sim}{0} \qquad (I.3)$$

Constitutive Equations

$$\underset{\sim}{\varepsilon} = \partial R/\partial\dot{\underset{\sim}{\tau}}; \quad \dot{\underset{\sim}{\tau}} = \frac{1}{2}(\dot{\underset{\sim}{t}}+\underset{\sim}{\tau}\cdot\underset{\sim}{\omega}-\underset{\sim}{\omega}\cdot\underset{\sim}{\tau}+\dot{\underset{\sim}{t}}^T); \qquad (I.4)$$

Velocity Boundary Condition (VBC)

$$\delta\underline{s}\cdot(-\underset{\sim}{\varepsilon}+\underset{\sim}{\omega}+\overline{\nabla\underline{V}}) = 0 \text{ on } S_V \;(\delta\underline{s} \text{ is any tangent on } S_V) \qquad (I.5)$$

Traction Boundary Condition (TBC)

$$\underline{n}\cdot\dot{\underset{\sim}{t}} = \dot{\overline{\underline{T}}}_t \text{ on } S_\sigma \qquad (I.6)$$

Above are listed the equations of the general boundary value problem associated with quasistatic deformations of inelastic solids. From (I.1) through (I.4) one may obtain 18 scalar equations for the 9 unknown stress rate components $\dot{t}^{ij}$, 3 unknown spin components ω^{ij}, and 6 unknown stretching components ε^{ij}. It is possible to reset (I.1) through (I.6) so that only velocity components V^i appear as variables. Alternatively one may use (I.4) to eliminate $\underset{\sim}{\varepsilon}$ as a variable in (I.1) and (I.3), thus obtaining a boundary value problem for the components of stress rate and spin. Any solution of this latter boundary value problem is a stationary point of the functional

$$\pi_{mc}(\underline{V},\underset{\sim}{\omega},\dot{\underset{\sim}{t}}) = \int_V \{-R - \frac{1}{2}\,\tau:(\underset{\sim}{\omega}\cdot\underset{\sim}{\omega}) + \dot{\underset{\sim}{t}}:\underset{\sim}{\omega}\}dV$$

$$+ \int_{S_V} \underline{n}\circ\dot{\underset{\sim}{t}}\cdot\overline{\underline{V}}dS + \int_{S_\sigma} (\underline{n}\cdot\dot{\underset{\sim}{t}}-\dot{\overline{\underline{T}}}_t)\cdot\underline{V}dS \qquad (I.7)$$

provided that only stress rate variations $\delta\underset{\sim}{\dot{t}}$ such that

$$\nabla \cdot \delta\underset{\sim}{\dot{t}} = \underline{0} \qquad (I.8)$$

and spin variations $\delta\underset{\sim}{\omega}$ such that

$$\delta\underset{\sim}{\omega} + \delta\underset{\sim}{\omega}^{T} = \underset{\sim}{0} \qquad (I.9)$$

are admitted to $\delta\pi_{mc}$. The velocity in $\delta\pi_{mc}$ plays the role of a Lagrange multiplier.

We replace the boundary value problem for $\underset{\sim}{\dot{t}}$ and $\underset{\sim}{\omega}$ by the generalized b.v.p.:

$$\delta\pi_{mc}(\underline{V},\underset{\sim}{\omega},\underset{\sim}{\dot{t}}) = 0 \qquad (I.10)$$

with subsidiary conditions:

$$\omega + \underset{\sim}{\omega}^{T} = \underset{\sim}{0} \qquad (I.11)$$

$$\nabla \cdot \underset{\sim}{\dot{t}} + \rho\dot{\underline{b}} = \underline{0} \qquad (I.12)^{*}$$

The stationary conditions of π_{mc}, when (I.11) and (I.12) decide admissible $\underset{\sim}{\omega}$ and $\underset{\sim}{\dot{t}}$, are

$$\int_V \{[(\underset{\sim}{\varepsilon}+\underset{\sim}{\omega}) \cdot \underset{\sim}{\tau} + \underset{\sim}{\dot{t}}]:\delta\underset{\sim}{\omega}\} = 0 \qquad (I.13)$$

$$\int_V \{[-\underset{\sim}{\varepsilon}+\underset{\sim}{\omega}]:\delta\underset{\sim}{\dot{t}}\}dV + \int_{S_V} \underline{n}.\delta\underset{\sim}{\dot{t}}.\underline{\bar{V}}dS = 0 \qquad (I.14)$$

$$\int_{S_\sigma} (\underline{n}.\underset{\sim}{\dot{t}}-\underline{\dot{\bar{T}}}_t) \cdot \delta\underline{V}dS = 0 \qquad (I.15)$$

where $\underset{\sim}{\varepsilon}$ is written for $\partial R/\partial\underset{\sim}{\dot{t}}$. Equations (I.13), (I.14), and (I.15) are variational statements of AMB (I.3), compatibility (I.1) and VBC (I.5), and TBC (I.6), respectively.

---

* the general solution of this equation is known as $\underset{\sim}{\dot{t}}=\underset{\sim}{\dot{t}}^{o}+\underset{\sim}{\dot{t}}^{b}$, where $\underset{\sim}{\dot{t}}^{o}=\nabla X\underset{\sim}{\Phi}$ and $\nabla.\underset{\sim}{\dot{t}}^{b}=-\rho\dot{\underline{b}}$.

Reformulation of the Constitutive Equation:

As may be surmised from the development above, the present approach necessitates reformulation of the constitutive equation. In applications one typically is given or may find a constitutive equation of the form

$$\dot{\underset{\sim}{\sigma}}{}^{*} = \underset{\approx}{V}:\underset{\sim}{\varepsilon} + \underset{\sim}{\Sigma} \qquad \text{(I.16)}$$

where $\underset{\approx}{V}$ and $\underset{\sim}{\Sigma}$ generally depend upon $\underset{\sim}{\varepsilon}$, $\underset{\sim}{\tau}$, and scalar invariants*. If $\underset{\approx}{V}$ and $\underset{\sim}{\Sigma}$ do not depend on $\underset{\sim}{\varepsilon}$ then we say (I.16) is affine with respect to $\underset{\sim}{\varepsilon}$. This includes most material models found in the engineering literature. If (I.16) is also an isotropic function then $\underset{\approx}{V}$ and $\underset{\sim}{\Sigma}$ may be set in the forms

$$\begin{aligned} V_{ijkl} = {} & \lambda^{11}(\delta_{ij}\delta_{kl}) + \lambda^{12}(\delta_{ij}\tau'_{kl}) + \lambda^{13}(\delta_{ij}s_{kl}) \\ & \lambda^{21}(\tau'_{ij}\delta_{kl}) + \lambda^{22}(\tau'_{ij}\tau_{kl}) + \lambda^{23}(\tau'_{ij}s_{kl}) \\ & \lambda^{31}(s_{ij}\delta_{kl}) + \lambda^{32}(s_{ij}\tau'_{kl}) + \lambda^{33}(s_{ij}s_{kl}) \\ & + 2\mu'(\delta_{ik\;jl}) + \mu^{2}(\delta_{ik}\tau'_{lj}+\tau'_{ik}\delta_{lj}) + \mu^{3}(\delta_{ik}s_{lj}+s_{ik}\delta_{lj}) \qquad \text{(I.17)} \end{aligned}$$

and $$\Sigma_{ij} = \eta^{1}\delta_{ij} + \eta^{2}\tau'_{ij} + \nu^{3}s_{ij} \qquad \text{(I.18)}$$

where $\underset{\sim}{\tau}'$ is the stress deviator and $\underset{\sim}{s}=\underset{\sim}{\tau}'.\underset{\sim}{\tau}'$. The λ^{IJ}, μ^{I}, and η^{I} are functions of the scalar invariants of the deformation.

This form still includes most material models found in the engineering literature. Notable exceptions are models for materials with anisotropy in the stress free state, where the present model reduces to

$$\dot{\underset{\sim}{\sigma}}{}^{*} = 2\mu^{1}\underset{\sim}{\varepsilon} + \lambda^{11}(\underset{\sim}{I}:\underset{\sim}{\varepsilon})\underset{\sim}{I} \qquad \text{(I.19)}$$

By retaining the constitutive equation in the general form (I.16), (I.17), (I.18) in our development we are led naturally to a 'unified numerical procedure' for problems of large strain elasticity, plasticity, viscoplasticity, and creep.

---

* temperature, strain histories, as well as joint invariants of $\underset{\sim}{\tau}$ and $\underset{\sim}{\varepsilon}$.

The desired form for the constitutive equation may be found by noting the relation between the stress rates $\underset{\sim}{\mathring{\sigma}}{}^*$ and $\underset{\sim}{\dot{r}}$:

$$\underset{\sim}{\dot{r}} = \underset{\sim}{\mathring{\sigma}}{}^* - \frac{1}{2}(\underset{\sim}{\tau}\cdot\underset{\sim}{\varepsilon}+\underset{\sim}{\varepsilon}\cdot\underset{\sim}{\tau}) \tag{I.20}$$

Using (I.16) to eliminate $\underset{\sim}{\mathring{\sigma}}{}^*$ from (I.20) gives

$$\underset{\sim}{\dot{r}} = (\underset{\approx}{V}:\underset{\sim}{\varepsilon}+\underset{\sim}{\Sigma}) - \frac{1}{2}(\underset{\sim}{\tau}\cdot\underset{\sim}{\varepsilon}+\underset{\sim}{\varepsilon}\cdot\underset{\sim}{\tau}) = \underset{\approx}{W}:\underset{\sim}{\varepsilon} + \underset{\sim}{\Sigma} \tag{I.21}$$

where $\underset{\approx}{W}$ is defined by

$$W_{ijkl} = V_{ijkl} - \frac{1}{2}(\tau_{ik}\delta_{lj}+\delta_{ik}\tau_{lj}) \tag{I.22}$$

Inversion of the relation (I.21) yields

$$\underset{\sim}{\varepsilon} = \underset{\approx}{W}^{-1}:(\underset{\sim}{\dot{r}}-\underset{\sim}{\Sigma}) \tag{I.23}$$

If $\underset{\approx}{W}^{-1}$ is symmetric (i.e., $W^{-1}_{ijkl}=W^{-1}_{klij}$) then a potential R exists for $\underset{\sim}{\varepsilon}$:

$$\underset{\sim}{\varepsilon} = \partial R/\partial\underset{\sim}{\dot{r}};\ R = \frac{1}{2}(\underset{\sim}{\dot{r}}-\underset{\sim}{\Sigma}):\underset{\approx}{W}^{-1}:(\underset{\sim}{\dot{r}}-\underset{\sim}{\Sigma}) \tag{I.24}$$

The condition necessary and sufficient for W^{-1} to be symmetric is $\lambda^{IJ}=\lambda^{JI}$. This condition is satisfied by most engineering materials*.

In practice one must construct $\underset{\approx}{W}$ from $\underset{\approx}{V}$, then invert $\underset{\approx}{W}$ (if possible) to achieve the form (I.24). This is a major undertaking from a computational point of view since $\underset{\approx}{W}$ is generally different at each point of a stressed body. Therefore special attention is given to practical methods for construction of $\underset{\approx}{W}^{-1}$. For plane problems $\underset{\approx}{W}^{-1}$ can be found analytically. For general problems in which $\underset{\approx}{V}^{-1}$ is known a simple approximation for $\underset{\approx}{W}^{-1}$ is often of acceptable accuracy. The details of the two special cases are discussed in Appendix B of [6].

The Finite Element Algorithm:

Equations (I.13), (I.14), and (I.15) are the basis for the finite element algorithm presented in this report. The finite element equations are obtained

---

* Flow laws using the corotational rate of the true stress are an exception.

by introduction of polynomial representations for $\underline{V}$, $\underset{\sim}{\omega}$, and $\dot{\underset{\sim}{t}}$* to (13) and (14); on the N^{th} element:

$$\underline{V} = \sum_{i=1}^{NQ} \underline{N}_i \, \tilde{q}_N^i \qquad \underline{N}_i\text{: isoparametric shape functions} \tag{I.25}$$

$$\underset{\sim}{\omega} = \sum_{i=1}^{NW} \underset{\sim}{QW}_i \alpha_N^i \qquad \text{where } \underset{\sim}{QW}_i + \underset{\sim}{QW}_i^T = 0 \tag{I.26}$$

$$\dot{\underset{\sim}{t}} = \sum_{i=1}^{NT} \underset{\sim}{QT}_i \beta_N^i + \dot{\underset{\sim}{t}}^b \qquad \text{where } \underset{\sim}{QT}_i = \nabla \times \underset{\sim}{\Phi}_i \tag{I.27}$$

$$\nabla . \dot{\underset{\sim}{t}}^b = -\rho \dot{\underline{b}}$$

The representations for $\underset{\sim}{\omega}$ and $\dot{\underset{\sim}{t}}$ are independent on each element, so (I.15) must be replaced by the 'interelement traction reciprocity' relation:

$$\sum_{N=1}^{NELM} \left\{ \int_{S_N \sim (S_N \cap S_V)} (\underline{n} . \dot{\underset{\sim}{t}} . \delta \underline{V}) \, dS - \int_{(S_N \cap S_\sigma)} \dot{\bar{\underline{T}}}_t . \delta \underline{V} dS \right\} = 0 \tag{I.28}$$

which includes (I.15). The finite element equations are obtained by performing the assigned integrations (Gaussian quadrature rules are used). Those equations are listed below (the element index 'N' has been suppressed on the α_N^i and β_N^i):

$$\{\delta\alpha\}^T \{ -[H^{11} \quad H^{12}] \begin{Bmatrix} \alpha \\ \beta \end{Bmatrix} + \{P^{\alpha,b}\} + \{P^{\alpha,\Sigma}\} \} = 0 \tag{I.29}$$

$$\{\delta\beta\}^T \{ -[H^{21} \quad H^{22}] \begin{Bmatrix} \alpha \\ \beta \end{Bmatrix} + \{P^{\beta,b}\} + \{P^{\beta,\Sigma}\} \tag{I.30}$$

$$+ [G]\{\tilde{q}_N\} \} = 0$$

$$\sum_{N=1}^{NELM} \{ \{\delta q_N\}^T [0 \quad G_N^T] \begin{Bmatrix} \alpha \\ \beta \end{Bmatrix} - \{\delta q_N\}^T \{F_N\} \} = 0 \tag{I.31}$$

---

*Mathematical 'rank' conditions require that $NT \geq NQ-T$, where T is the number of translational degrees of freedom of an element. Moreover, the [QW] and [QT] should be of the same polynomial degree.

Henceforth we refer to (I.29) as AMB, to (I.30) as compatibility, and to (I.31) as TBC. The individual matrices are defined below:

$$H^{11}_{ij} = \int_{V_N} \{(\underset{\sim}{\tau}.\underset{\sim}{QW}_i):\underset{\approx}{D}:(\underset{\sim}{\tau}.\underset{\sim}{QW}_j) + \underset{\sim}{\tau}:(\underset{\sim}{QW}_i\ \underset{\sim}{QW}_j)\}dV \tag{(.32}$$

$$H^{12}_{ij} = \int_{V_N} \{(\underset{\sim}{\tau}.\underset{\sim}{QW}_i):\underset{\approx}{D}:(\underset{\sim}{QT}_j) - \underset{\sim}{QW}_i:\underset{\sim}{QT}_j\}dV \tag{I.33}$$

$$H^{21}_{ij} = \int_{V_N} \{(\underset{\sim}{QT}_i):\underset{\approx}{D}:(\underset{\sim}{\tau}.\underset{\sim}{QW}_j) - \underset{\sim}{QT}_i:\underset{\sim}{QW}_j\}dV \tag{I.34}$$

$$H^{22}_{ij} = \int_{V_N} \{(\underset{\sim}{QT}_i):\underset{\approx}{D}:(\underset{\sim}{QT}_j)\}dV \tag{I.35}$$

$$G_{ij} = \int_{S_N} \underline{n}.(\underset{\sim}{QT}_i).(\underline{N}_j)dS \tag{I.36}$$

$$F_i = \int_{(S_N \cap S_\sigma)} \dot{\underline{T}}_t.(\underline{N}_i)dS \tag{I.37}$$

$$P^{\alpha,b}_i = \int_{V_N} \{(\underset{\sim}{QW}_i):[\dot{\underset{\sim}{t}}^b+(\underset{\approx}{D}:\dot{\underset{\sim}{t}}^b).\underset{\sim}{\tau} + \frac{1}{h}\underset{\sim}{\tau}]\}dV \tag{I.38}$$

$$P^{\beta,b}_i = \int_{V_N} \{(\underset{\sim}{QT}_i):(-\underset{\approx}{D}:\dot{\underset{\sim}{t}}^b)\}dV \tag{I.39}$$

$$P^{\alpha,\Sigma}_i = \int_{V_N} \{(\underset{\sim}{\tau}.\underset{\sim}{QW}_i):\underset{\approx}{D}:\underset{\sim}{\Sigma}\}dV \tag{I.40}$$

$$P^{\beta,\Sigma}_i = \int_{V_N} \{(\underset{\sim}{QT}_i):\underset{\approx}{D}:\underset{\sim}{\Sigma}\}dV \tag{I.41}$$

and $\underset{\approx}{D}$ is obtained from $\underset{\approx}{W}^{-1}$ by symmetrization:

$$D_{ijkl} = \frac{1}{4}(W^{-1}_{ijkl} + W^{-1}_{jikl} + W^{-1}_{ijlk} + W^{-1}_{jilk}) \tag{I.42}$$

---

*The last term in the integrand is a residual whose significance is explained in [6].

This symmetrization is easily done after $\underset{\approx}{W}^{-1}$ is computed, and serves to reduce by a factor of four the number of multiplications required to compute the H matrices (I.32) through (I.35), and other matrices involving $\underset{\approx}{W}^{-1}$.

The procedure which leads one from equations (I.29) and (I.30) to the element stiffness matrix is virtually identical to that of Pian [1]. We define the element 'H-matrix' as

$$[H] = \begin{bmatrix} H^{11} & H^{12} \\ H^{21} & H^{22} \end{bmatrix} \tag{I.43}$$

and loads $\{P^b\}$ and $\{P^\Sigma\}$, due to body force and fluidity, respectively, as

$$\{P^b\} = \begin{Bmatrix} P^{\alpha,b} \\ P^{\beta,b} \end{Bmatrix} : \{P^\Sigma\} = \begin{Bmatrix} P^{\alpha,\Sigma} \\ P^{\beta,\Sigma} \end{Bmatrix} \tag{I.44}$$

Then (I.29) and (I.30) may be collected into a single equation as

$$[H]\begin{Bmatrix} \alpha \\ \beta \end{Bmatrix} = \begin{bmatrix} 0 \\ G \end{bmatrix} \{\tilde{q}\} + \{P^b + P^\Sigma\} \tag{I.45}$$

If $\underset{\approx}{D}$ is symmetric, that is, if $W^{-1}_{ijkl}=W^{-1}_{klij}$, then from (I.32) through (I.35) we easily determine that [H] is symmetric.

If the H-matrix is not singular, then we solve the matrix equation (NQ+1 right hand sides)

$$[H][H^{-1}G \quad H^{-1}P] = \left[\begin{array}{c|c} 0 & \\ & P^b + P^\Sigma \\ G & \end{array}\right] \tag{I.46}$$

on each element. Explicit calculation of the inverse of [H] is not only unnecessary, but substantially increases the time required to generate the element stiffness matrix. According to (I.45), the spin and stress parameters on each element are given by

$$\begin{Bmatrix} \alpha \\ \beta \end{Bmatrix} = [H^{-1}G]\{\tilde{q}\} + \{H^{-1}P\} \tag{I.47}$$

Using (I.47) to eliminate $\{\alpha/\beta\}$ from TBC (I.31) leads to

$$\sum_{N=1}^{NELM} \{\{\delta q_N\}^T[K_N]\{\tilde{q}_N\} + \{\delta q_N\}[0 \quad G_N^T]\{H^{-1}P_N\} - \{\delta q_N\}^T\{F_N\}\} = 0 \qquad (I.48)$$

in which the element stiffness matrix has been identified as

$$[K_N] = [0 \quad G_N^T][H^{-1}G_N] \qquad (I.49)$$

and the resultant nodal 'forces' are given by

$$-[0 \quad G_N^T]\{H^{-1}P_N\} + \{F_N\} \qquad (I.50)$$

It is easily verified that the element stiffness matrix [K] is symmetric if [H] is, and so the symmetry of [K] ultimately depends upon the symmetry of the constitutive matrix $\underset{\approx}{W}$.

To this point all of the finite element equations are independent on each element. The formal assembly of the global stiffness matrix and loads is accomplished by introduction of assembly matrices $[A_N]$ through whose use the element level velocity parameters may be expressed as functions of the global velocity parameters. For $\{\tilde{q}\}$ and $\{\delta q\}$ we write

$$\{\tilde{q}_N\} = [A_N]\{Q+\bar{Q}\}: \quad \{\delta q_N\} = [A_N]\{\delta Q\};$$

and from (I.48) thus obtain

$$\{\delta Q\}^T[K_G]\{Q\} = \{\delta Q\}^T\{P_G\} - \{\delta Q\}^T[K_G]\{\bar{Q}\} \qquad (I.51)$$

In equation (I.51) the global stiffness matrix $[K_G]$ and the loads $\{P_G\}$ are defined by

$$[K_G] = \sum_{N=1}^{NELM} [A_N]^T[K_N][A_N] \qquad (I.52)$$

and $$\{P_G\} = [A_N]^T\{\{F_N\} - [0 \quad G]\{H^{-1}P_N\}\} \qquad (I.53)$$

The load matrix $\{P_G\}$ contains contributions from the prescribed body for rate $\dot{\underline{b}}$, the relaxation $\underset{\sim}{\Sigma}$, and the traction boundary condition $\dot{\bar{\underline{T}}}_t$. The global stiffness matrix, as defined by (I.52), will be singular for rigid translations (but not for rigid spin). In order to solve the equation (I.51) we define a modified global stiffness matrix [K*] and a modified load {P*} as follows:

$$K^*_{IJ} = \begin{cases} \delta_{IJ} \text{ if } (\tilde{Q}_I=\overline{Q}_I) \text{ or } (\tilde{Q}_J=\overline{Q}_J) \\ K_{IJ} \text{ otherwise} \end{cases} \tag{I.54}$$

$$P^*_I = \begin{cases} Q_I \text{ if } (\tilde{Q}_I=\overline{Q}_I) \\ P_I - \sum_{J=1}^{NELM} K^G_{IJ}\overline{Q}_J \text{ otherwise} \end{cases} \tag{I.55}$$

Then (I.51) may be replaced by

$$[K^*]\{\tilde{Q}\} = \{P^*\} \tag{I.56}$$

If [K*] is not singular, then we solve (I.56) for $\{\tilde{Q}\}$,

$$\{\tilde{Q}\} = [K^*]^{-1}\{P^*\} \tag{I.57}$$

By backsubstitution we obtain the velocity (on the boundary of each element), the spin and the stress rate on each element:

$$\{\tilde{q}_N\} = [A_N][K^*]^{-1}\{P^*\} \tag{I.58}$$

$$\left\{\begin{matrix}\alpha_N\\ \beta_N\end{matrix}\right\} = [H^{-1}G_N][A_N][K^*]^{-1}\{P^*\} + \{H^{-1}P_N\} \tag{I.59}$$

$$\underline{v}(\underline{x}) = [\underline{N}(\underline{x})][A_N][K^*]^{-1}\{P^*\} \tag{I.60}$$

$$\left\{\begin{matrix}\underset{\sim}{\omega}(\underline{x}) \\ \underset{\sim}{\dot{t}}(\underline{x}) - \underset{\sim}{t}^b(\underline{x})\end{matrix}\right\}_N = \begin{bmatrix} Q\underset{\sim}{W}(\underline{x}) & 0 \\ 0 & Q\underset{\sim}{T}(\underline{x}) \end{bmatrix} \left\{[H^{-1}G_N][A_N][K^*]^{-1}\{P^*\} + \{H^{-1}P_N\}\right\} \tag{I.61}$$

Equations (I.60) and (I.61) comprise the approximate solution of the boundary value probelm.

Integration of the Motion of the Body:

The finite element algorithm just described produces an approximation for the stress rate and velocity, as opposed to stress increments and displacement increments. Thus, considerably more freedom of choice of time integration schemes is afforded by the present approach than by incremental approaches (which are predisposed to integration by the relatively inefficient Euler's method). In this section we (i) formally state the initial value problem, (ii) discuss numerical integration of that problem, and (iii) present a 'forward gradient scheme' which stabilizes integration of deformations of bodies which exhibit stress relaxation.

Let $\{\underline{x}\} = \{\underline{x}^1, \underline{x}^2, \ldots, \underline{x}^{ND}\}$ be the vector of nodal positions, and let $\{\underline{v}\} = \{\underline{v}^1, \underline{v}^2, \ldots, \underline{v}^{ND}\}$ be the vector of <u>nodal velocities</u>, where ND is the total number of nodes. Similarly, let $\{\underset{\sim}{\tau}\} = \{\underset{\sim}{\tau}^1, \underset{\sim}{\tau}^2, \ldots, \underset{\sim}{\tau}^G\}$ and $\{\dot{\underset{\sim}{t}}\} = \{\dot{\underset{\sim}{t}}^1, \dot{\underset{\sim}{t}}^2, \ldots, \dot{\underset{\sim}{t}}^G\}$ be the quadrature point stresses and stress rates, respectively, where G is the total number of quadrature points in the body. To indicate the dependence of $\{\underline{v}\}$ and $\{\dot{\underset{\sim}{t}}\}$ on $\{\underline{x}\}$, $\{\underset{\sim}{\tau}\}$, and the time dependent prescribed loads, we write*

$$\{\underline{v}\} = f[\{\underline{x}\}, \{\underset{\sim}{\tau}\}, t\} \qquad (I.62)$$

$$\{\dot{\underset{\sim}{t}}\} = g[\{\underline{x}\}, \{\underset{\sim}{\tau}\}, t\} \qquad (I.63)$$

Since each element node is associated with the same material point $\underline{X}^I$ throughout a deformation, and likewise for each quadrature point, we may write each component of $\{\underline{x}\}$, $\{\underset{\sim}{\tau}\}$, $\{\underline{v}\}$, and $\{\dot{\underset{\sim}{t}}\}$ as

$$\underline{x}^I = \underline{\chi}_\tau(\underline{X}^I, t) \qquad (I.64)$$

$$\underset{\sim}{\tau}^I = (1/J^I_\tau)\underset{\sim}{F}^I_\tau \cdot \underset{\sim}{t}_\tau(\underline{X}^I, t) \qquad (I.65)$$

$$\underline{v}^T = \dot{\underline{\chi}}_\tau(\underline{X}^I, t) \qquad (I.66)$$

$$\dot{\underset{\sim}{t}}^I = (1/J^I_\tau)\underset{\sim}{F}^I \cdot \dot{\underset{\sim}{t}}_\tau(\underline{X}^I, t) \qquad (I.67)$$

---

* The function f and g are introduced specifically as a 'shorthand' for the solution of the finite element equations, as given by (I.60) and (I.61). In practice integrations may be performed on one element at a time.

Introduction of (I.64) - (I.67) to (I.62) and (I.63) gives

$$\{\dot{\underline{\chi}}_\tau\} = f_\tau[\{\underline{\chi}_\tau\}, \{\underset{\sim}{t}_\tau\}, t] \tag{I.68}$$

$$\{\dot{\underset{\sim}{t}}_\tau\} = g_\tau[\{\underline{\chi}_\tau\},\{\underset{\sim}{t}_\tau\}, t] \tag{I.69}$$

the definitions of f_τ and g_τ being clear. Equations (I.68) and (I.69) and appropriate initial values comprise an initial value problem.

The initial value problem posed by (I.68) and (I.69) and appropriate initial data is dependent upon the finite element equations. From that same discussion, and from the presentation of the finite element equations, it is also clear that the finite element-initial value problem is predisposed to numerical integration. In this section we indicate the types of numerical integration schemes suitable for the present problem, and mention a few important differences between the various types.

The finite element-initial value problem may be integrated by single step explicit schemes, multistep explicit schemes, or (generally multistep) predictor-corrector schemes. Three important facts to be kept in mind when choosing a particular scheme are

(i) the solution vector $<\{\underline{\chi}_\tau(t_N)\}, \{\underset{\sim}{t}_\tau(t_N)\}>$ at the time $t=t_N$ is of scalar dimension NDOF+9.G, where NDOF is the number of kinematic degrees of freedom of the mesh and G is the total number of quadrature points. Storage required for implementation or different integration schemes can vary appreciably.

(2) evaluation of $<f_\tau, g_\tau>$ is expensive on account of the complexity of the finite element equations.

(3) the functions f_τ and g_τ are generally discontinuous at points $<\underline{\chi}_\tau, \underset{\sim}{t}_\tau>$ which correspond to material yield surfaces.

The multistep methods (explicit and predictor-corrector) require relatively few evaluations of $<f_\tau, g_\tau>$ per step; this is an attractive feature.

However, multistep methods are not self starting, the time step is not easily changed, they have relatively large storage requirements (since several past values of $\langle f_\tau, g_\tau \rangle$ must be carried along), and moreover, they cannot be expected to be accurate when the solution crosses a yield surface (since they are based on smooth polynomial interpolation of the solution over several time steps).

On the other hand, the single step methods (explicit and predictor-corrector) are easily started, the time step size is easily adjusted, and they have relatively small storage requirements. They can be expected to perform more favorably than the multistep methods when the solution crosses a yield surface since smoothing over several time steps is not built in. The disadvantage of the single step methods is that a relatively larger number of evaluations of $\langle f_\tau, g_\tau \rangle$ are required per step to achieve a given accuracy when a yield surface is not crossed. However, the advantage of single step methods seem to far outweigh the disadvantages.

In the example accompanying this report the Euler and classical second order Runge-Kutta methods were used. Details of these methods may be found in many textbooks. Errors of the Euler method were gauged (qualitatively) by step-halving and by comparison to results of second order integration for randomly selected time steps. Full details are given in the description of the example problem.

It is worthy of special note that complementary work and energy principles provide no means whatever for checking the satisfaction of LMB, so it is of crucial importance that the numerical integration scheme not introduce errors which tend to unbalance the stress. This maintenance of balanced stress, necessary in stress-based finite element algorithms is the counterpart of maintenance of compatible deformation, necessary in velocity - based algorithms. It can be shown that LMB is maintained when the stress $\underset{\sim}{t}_\tau$ is integrated explicitly, but not when other stresses (such as $\underset{\sim}{\tau}$) are integrated explicitly. Thus, we integrate $\underset{\sim}{t}_\tau$ explicitly, and find $\underset{\sim}{\tau}$ (afterwards) by the formula

$$\underset{\sim}{\tau} = 1/J_\tau \underset{\sim}{F}_\tau \cdot \underset{\sim}{t}_\tau \qquad \text{(I.70)}$$

Stability of Numerical Integration of the Initial Value Problem:

It is possible that the difference between two supposed numerical solutions of a given initial value problem is much larger than would be expected to arise from discretization error alone. As an example, consider integration of the stress in a material of the type (I.16) by the Euler method. We suppose, for the sake of simplicity, that $\underset{\sim}{\varepsilon}(t)$ is given and $\underset{\sim}{\Sigma}(\underset{\sim}{\tau}) = -2\mu(\frac{3}{2}\gamma\underset{\sim}{\tau}')$, so that the difference between two solutions satisfies

$$\Delta\underset{\sim}{\overset{\circ}{\sigma}}{}^* = [\underset{\approx}{V}(\underset{\sim}{\tau} + \Delta\underset{\sim}{\tau}) - \underset{\approx}{V}(\underset{\sim}{\tau})]:\underset{\sim}{\varepsilon}(t) - (3\mu\gamma)\Delta\underset{\sim}{\tau}' \qquad \text{(I.71)}$$

If the elastic matrix and stretching are such that, in the Euclidean norm,

$$||[\underset{\approx}{V}(\underset{\sim}{\tau}+\Delta\underset{\sim}{\tau}) - \underset{\approx}{V}(\underset{\sim}{\tau})]:\underset{\sim}{\varepsilon}(t)||/||\Delta\underset{\sim}{\tau}|| \to 0 \qquad \text{(I.72)}$$

as $||\Delta\underset{\sim}{\tau}|| \to 0$, then for sufficiently small $||\Delta\underset{\sim}{\tau}||$, equation (I.71) may be replaced by

$$\Delta\underset{\sim}{\overset{\circ}{\sigma}}{}^* = -(3\mu\gamma)\Delta\underset{\sim}{\tau}' \qquad \text{(I.73)}$$

Defining $\Delta\sigma$ as $\Delta\sigma = J_o\sqrt{\frac{3}{2}\Delta\underset{\sim}{\tau}':\Delta\underset{\sim}{\tau}'}$, we may reduce (I.73) to a scalar equation in the invariant $\Delta\sigma$:

$$\frac{d}{dt}(\Delta\sigma) = -(3\mu\gamma)\Delta\sigma \qquad \text{(I.74)}$$

For an initial value $\Delta\sigma(0)$ (small), the analytic solution of (I.74) is

$$\Delta\sigma(t) = \Delta\sigma(0)e^{-(3\mu\gamma)t} \qquad \text{(I.75)}$$

Euler's method yields

$$\Delta\sigma_N = \Delta\sigma(0)(1-3\mu\gamma h)^N \qquad \text{(I.76)}$$

It is clear from (I.75) that $\Delta\sigma$ decays to zero as time passes. This means that the analytic solution of the equation

$$\underset{\sim}{\overset{\circ}{\sigma}}{}^* = \underset{\approx}{V}:\underset{\sim}{\varepsilon}(t) + \underset{\sim}{\Sigma};\ \underset{\sim}{\tau}(0) = \underset{\sim}{\tau}_o \qquad \text{(I.77)}$$

is stable with respect to sufficiently small perturbations of the deviatoric part of $\underset{\sim}{\tau}$. On the other hand, the numerical solution (I.76) attenuates as time passes only if

$$|(1 - 3\mu\gamma h)| < 1 \qquad \text{(I.78)}$$

This means that the numerical solution of (I.77) is stable with respect to small perturbations of the deviatoric part of $\underset{\sim}{\tau}'$ only so long as the time step h is bounded above as

$$|h| < 2/(3\mu\gamma) \qquad \text{(I.79)}$$

This bound is identical to the bound given by Cormeau [7] (see equations 16 and 54 in this reference).

Time steps such as (I.79) are found to be necessary for stability of numerical solutions of the finite element-initial value problem presented in this report. Argyris et al [8] remark that this time step restriction amounts to limiting the inelastic strain increment to be smaller than the elastic strain. Since the elastic strain is usually very small in metals such as those used in structures, this implies that a finite deformation analysis would entail an impractically large number of steps.

The work of Kanchi et al [9] and Atluri and Murakawa [4] suggests the modification we now describe. To improve the estimate of the inelastic strain increment in a time step, we replace $\underset{\sim}{\varepsilon}^P(\underset{\sim}{\tau}_N)$ by an estimate of the mean value of the inelastic stretching in that time step:

$$\underset{\sim}{\varepsilon}^P(\underset{\sim}{\tau}(t_N+\theta h)) \doteq \underset{\sim}{\varepsilon}^P(\underset{\sim}{\tau}(t_N)) + \theta h \left.\frac{d\underset{\sim}{\varepsilon}^P}{d\underset{\sim}{\tau}}\right|_{\underset{\sim}{\tau}=\underset{\sim}{\tau}_N} : \underset{\sim}{\dot{\sigma}}^* \qquad \text{(I.80)}$$

where the parameter θ, $0 \leq \theta \leq 1$, serves to locate the time at which the mean value is achieved. As θ goes from zero to one, the estimate of the creep-stretch becomes increasingly more conservative.

Equation (I.80) may be introduced to the finite element algorithm through the constitutive equation; (I.16) becomes

$$\underset{\sim}{\dot{\sigma}}^{*} = \underset{\approx}{V}_{\theta} : \underset{\sim}{\varepsilon} + \underset{\sim}{\Sigma}_{\theta}$$

where

$$\underset{\approx}{V}_{\theta} = \left[\underset{\approx}{V}^{-1} + \theta h \frac{d\underset{\sim}{\varepsilon}^{p}}{d\underset{\sim}{\tau}}\right]^{-1} ; \quad \underset{\sim}{\Sigma}_{\theta} = -\underset{\approx}{V}_{\theta} : \underset{\sim}{\varepsilon}^{p} \qquad \text{(I.81)}$$

From $\underset{\approx}{V}_{\theta}$ (I.81) we derive $\underset{\approx}{W}_{\theta}$ just as we derived $\underset{\approx}{W}$ from $\underset{\approx}{V}$:

$$\underset{\approx}{\dot{W}}_{\theta} = \underset{\approx}{V}_{\theta} - \underset{\approx}{T} ; \quad T_{ijkl} = \frac{1}{2}(\tau_{ik}\delta_{lj} + \delta_{ik}\tau_{lj}) ;$$

$$\underset{\sim}{\Sigma}_{\theta} = -\underset{\approx}{V}_{\theta} : \underset{\sim}{\varepsilon}^{p} = -(\underset{\approx}{W}_{\theta} + \underset{\approx}{T}) : \underset{\sim}{\varepsilon}^{p} \qquad \text{(I.82)}$$

When a material which exhibits relaxation is to be analyzed, $\underset{\approx}{W}_{\theta}$ and $\underset{\sim}{\Sigma}_{\theta}$ are introduced to the finite element algorithm for $\underset{\approx}{W}$ and $\underset{\sim}{\Sigma}$.

Example: Growth of a Void in a Viscoplastic Medium:

In this example we examine the growth of a void in a hypoelastic/viscoplastic medium. This problem has been studied (numerically) by Burke and Nix [10], who treated the material as rigid/viscoplastic. We present the problem as a demonstration of the performance of the finite element algorithim. The material exhibits stress relaxation, so the forward gradient scheme must be used to stabilize the time integration. The present results agree quite closely with those of Burke and Nix.

The motion is assumed to be plane strain, and throughout the body is a doubly periodic array of cylinderical voids. Due to the symmetry we need analyse only one quadrant of one rectangular cell of the body. The finite element mesh and boundary conditions are described in Figure 1.

Burke and Nix motivate their study by explaining that certain theories for the initiation of creep fracture supose that the growth of voids can be "attributed to the inhomogeneous plastic deformation of the surrouding grains." Furthermore, "finite fracture strains can be predicted only when a void lies in the neighborhood of another void." Such a study necessarily involves a number of special cases. For our purposes, that of demonstration, only one case is taken.

The problem has been analysed in three parts. In the first part the cell is brought rapidly from the virgin state (stress-free) to a state of purely elastic strain. This is accomplished by a single RK2 step. In the second part, relatively small time steps are taken while the stress relaxes from the elastic distribution to a nearly steady creep distribution. In the third part, time steps are taken which produce 1% nominal elongation of the cell in each step. To stabilize time integration in the second and third parts the forward gradient scheme is used, the stability parameter θ set as $\theta = 1/2$ and $3/4$. Only the Euler time stepping scheme has been used in the second and third parts of the problem.

The material model is a special case of (I.16):

$$\underset{\sim}{\varepsilon} = \underset{\sim}{\varepsilon}^{e} + \underset{\sim}{\varepsilon}^{p}$$

$$\underset{\sim}{\varepsilon}^{e} = \left(\frac{1+\nu}{E}\right)\underset{\sim}{\dot{\sigma}}^{*} - \left(\frac{\nu}{E}\right)(\underset{\sim}{I}:\underset{\sim}{\dot{\sigma}}^{*})\underset{\sim}{I}$$

$$\underset{\sim}{\varepsilon}^{p} = \frac{3}{2}\gamma\underset{\sim}{\tau}'$$

This model corresponds to that of Burke and Nix with (their) creep exponent n=1. The fluidity γ is set as $\gamma=1\text{x}10^{-19}$ $(\text{psi-sec})^{-1}$. The velocity at the top of the cell (see Figure 1) was adjusted so that a specimen with no void would experience a homogeneous constant stretching $\bar{\varepsilon}^{11}$ of $\bar{\varepsilon}^{11}=0.25\text{x}10^{-14}$ sec.^{-1}. Since the material was treated as rigid/viscoplastic by Burke and Nix, our choice of elastic constants is somewhat arbitrary. We have taken Young's modulus $E=3\text{x}10^{7}$ psi and Poisson ratio $\nu=0.4$, so the material is somewhat like steel in its elastic response.

In Figures 2, 3, and 4 the contours of stress τ^{11}, stress τ^{33} and mean stress, have been plotted for L (the elongation of the cell) L=1.01. The stress concentration where the hole edge crosses the x^3 axis is approximately 2.7*. This is quite reasonable since the theoretical value for an isolated void in a purely elastic medium is 3.0. In Reference 10 an approximate value of 2.66 was found for the rigid plastic material. In Figure 5 the contours of effective strain rate $\sqrt{\frac{2}{3}\underset{\sim}{\varepsilon}^p : \underset{\sim}{\varepsilon}^p}$ are plotted for L=1.01. Qualitatively this compares very well to Figure 7 in [10].

In Figure 6 the deformation is traced from L=1.0 to L=1.5. These deformations are physically tenable. We remark that no indication of any numerical instability was observed in the course of integrating this deformation.

In Figures 7, 8, and 9 the contours of stress τ^{11}, τ^{33}, and mean stress, have been plotted for L=1.50. They compare very well to the stresses found in [10] (see Figure 8 there). We note that the stress concentration has dropped to 1.71. The stress concentration depends strongly on the geometry of the specimen; as such, it was observed to decline steadily throughout the deformation. In Figure 10 the contours of effective strain rate are plotted for L=1.5. Again, the qualitative agreement with the results of Burke and Nix [10] is noted (see Figure 9 there).

We conclude by noting that in the present analysis only 56 four noded elements were used, as compared to 56 eight noded elements used in the analysis of Burke and Nix. Considering the agreement between their results and our own, the present method appears to have performed very well, in spite of the large disparity in the degrees of freedom of the finite element mesh.

---

* A stress concentration of approximately 2.59 was observed for the elastically stressed medium.

Part II: Fracture Analyses Under Creep

Numerous experimental studies have been undertaken with the purpose of finding a parameter which correlates with creep crack propagation rate. Most of these investigations consider as candidate parameters, K_I, some form of net section (or reference) stress or in more recent studies C*. See, for example, the review article [11] and [12-14]. Since the introduction of C*, there appears to be less emphasis on K_I as a parameter, however, there are apparently real materials and conditions for which either net section stress or K_I provide better correlation with crack growth rate than C*.

As illustrated in Fig. 11, the above three parameters might be expected to correlate three distinctly different creep crack growth situations. In Fig. 11a, a crack and its associated ligament are shown for a material and geometry which results in negligible creep strains everywhere except in the vicinity of the crack-tip. This condition is analogous to that of small scale yielding in elastic-plastic fracture.

Fig. 11b represents a situation in which C* might be considered an appropriate parameter. This situation is characterized (i) by the body being essentially at steady-state creep conditions (which implies very slow crack propagation) and (ii) by the creep-damage process-zone being local to and therefore controlled by the crack-tip field. Fig. 11c illustrates the type of situation for which net section stress might be expected to control crack growth. In this case, the main feature is the widespread creep damage zone.

It is seen from Fig. 11 that intermediate situations can occur. For example, suppose a particular material and geometry results in a crack propagation rate such that elastic strain rates are not negligible compared to creep rates (i.e., non-steady creep) and at the same time, creep strains are no longer localized to the crack-tip region. While neither K_I nor C* could be valid parameters for this case, it appears reasonable to expect that crack growth rate is still determined by the local crack-tip field since the creep damage process zone is still assumed to be local to the crack-tip.

In the present study, we are concerned primarily with behavior bounded by at illustrated in Fig. 11a and Fig. 11b. That is, we consider conditions in which the creep damage zone and presumably crack propagation speed are controlled by the crack-tip field. Therefore, if we have a parameter which characterizes the crack-tip fields during such behavior we presumably have a parameter which will characterize creep crack propagation rate. A parameter which spans the gap between K_I controlled growth and C* controlled growth has been introduced in [15] and subjected to initial scrutiny in [16]. This parameter is referred to as $(\Delta \underline{T})_c$ and is defined by a path-independent, vector integral. For stationary cracks, it has been shown [15,16] that the related quantity $(\dot{\underline{T}})_c$ is a measure of the amplitude of the HRR crack-tip field which presumably exists for both non-steady and steady-state creep. It has also been shown that $(\dot{T}_1)_c$ has the energy interpretation $(\dot{T}_1)_c = -\frac{d\dot{U}}{da}$ for non-steady as well as steady-state creep.

In the process of exploring this new parameter, it has been found [16] that despite C* being a valid crack-tip parameter for strictly steady-state creep conditions, it is not equivalent to the $(\dot{T}_1)_c$ parameter under any conditions and therefore does not have the energy interpretation commonly attributed to it. Since experimentalists use the energy interpretation as a means of "measuring" C* it seems more appropriate to refer to these experimental results as $(\dot{T}_1)_c$.

To start with, we define $(\Delta \underline{T})_c$ and a generalized vector integral $\underline{C}^*$ and also summarize the properties and the relationship of these parameters. The remainder of the paper discusses several finite element calculations for both stationary cracks and propagating cracks. The crack propagation study uses a combination of analytical, numerical and experimental results to show that creep crack growth in 304 stainless steel at 650°C occurs under essentially steady-state creep conditions. Finally, based on this observation, a simple crack growth prediction methodology is outline.

Constitutive Equations:

In this study we assume strains are infinitesimal and the deformations small. Furthermore, we assume material behavior of the type:

$$\dot{\epsilon}_{ij} = \dot{\epsilon}^{e}_{ij} + \dot{\epsilon}^{c}_{ij} = C_{ijk\ell}\dot{\tau}_{k\ell} + \frac{3}{2}\gamma(\bar{\sigma})^{n-1}\tau'_{ij} \tag{II.1}$$

where $\dot{\epsilon}^{e}_{ij}$ and $\dot{\epsilon}^{c}_{ij}$ are the elastic and creep strain rates, respectively, $C_{ijk\ell}$ is the tensor of elastic moduli, $\dot{\tau}_{k\ell}$ is the stress rate, τ'_{ij} is the deviatoric stress ($\tau'_{ij}=\tau_{ij}-\frac{1}{3}\tau_{kk}\delta_{ij}$), and $\bar{\sigma}$ is the equivalent stress given by $\bar{\sigma}=(3/2)(\tau'_{ij}\tau'_{ij})^{1/2}$. The parameters γ and n are those of the familiar Norton power law:

$$\dot{\bar{\epsilon}} = \gamma(\bar{\sigma})^{n} \tag{II.2}$$

where

$$\dot{\bar{\epsilon}} = [(2/3)\dot{\epsilon}_{ij}\dot{\epsilon}_{ij}]^{1/2}$$

The constitutive law (II.1) can result in steady-state creep response (i.e., $\dot{\tau}_{ij}\equiv 0$) after some period of time provided the boundary conditions are some combination of time invariant tractions or time invariant displacement rates.

Fracture Parameters $(\Delta \underline{T})_c$ and $\underline{C}^*$:

We now define two vector quantities which have applications to fracture analysis under creep conditions. The first quantity is $(\Delta \underline{T})_c$ as recently defined by Atluri [15] and subsequently examined in greater detail in [16]. In [15] $(\Delta \underline{T})_c$ is defined in the context of finite strains and large deformations. Here we give the corresponding definition for infinitesimal strains and small deformations.

$$\begin{aligned}(\Delta T_i)_c \equiv \underset{\epsilon\to 0}{\mathrm{Lt}} \int_{\Gamma_\epsilon} & [n_i \Delta W - n_j(\tau_{jk}+\Delta\tau_{jk}) \frac{\partial \Delta u_k}{\partial x_i}] dS \\ = \int_{\Gamma_{234}} & [n_i \Delta W - n_j(\tau_{jk}+\Delta\tau_{jk}) \frac{\partial \Delta u_k}{\partial x_i}] dS \\ + \underset{\epsilon\to 0}{\mathrm{Lt}} & \left\{ \int_{V-V_\epsilon} [\rho(a_k - f_k)\frac{\partial \Delta u_k}{\partial x_i} - \frac{\partial \tau_{jk}}{\partial x_i}\Delta\epsilon_{jk}] dV \right. \\ & + \int_{\Gamma_{12}} n_i \Delta W dS + \int_{\Gamma_{45}} n_i \Delta W dS - \int_{S_t} \bar{t}_k \frac{\partial \Delta u_k}{\partial x_i} dS \\ & \left. - \int_{S_e} n_j(\tau_{jk}+\Delta\tau_{jk}) \frac{\partial \Delta \bar{u}_k}{\partial x_i} dS \right\} \end{aligned} \qquad \text{(II.3)}$$

The various contour integral paths and their outward unit normals $\underline{n}$ as well as V and V_ϵ are illustrated in Fig.12 for a two-dimensional, cracked body. In writing (II.3) it has been assumed that $S_e+S_t=\Gamma_{12}+\Gamma_{45}$ where S_e and S_t are the portions of the crack surfaces with applied incremental displacements, $\Delta\bar{u}_k$, and applied tractions $\bar{t}_k$, respectively. The initial stress for the increment is denoted τ_{jk}. The mass density is ρ and the acceleration and body force components at the end of the increment are a_k and f_k, respectively. The quantity ΔW is the incremental stress-working density and is given by

$$\Delta W = (\tau_{ij} + \frac{1}{2}\Delta\tau_{ij})\Delta\epsilon_{ij} \qquad \text{(II.4)}$$

The right equality of (II.3) shows that $(\Delta T_i)_c$ is independent of the selection of Γ_{234} (provided the fields within $V-V_\epsilon$ are sufficiently well behaved for the divergence theorem to be applicable). It is important to note that this path-independence exists during non-steady as well as steady-state creep.

In the present study we consider cracks along the x_1 axis and symmetrical, Mode I type deformations. Furthermore, we consider traction-free crack surfaces and assume body forces and accelerations are negligible. Under these conditions, only $(\Delta T_1)_c$ is of interest and we have

$$(\Delta T_1)_c = \int_{\Gamma_{234}} [n_1 \Delta W - n_j(\tau_{jk}+\Delta\tau_{jk}) \frac{\partial \Delta u_k}{\partial x_1}] dS - \int_V \frac{\partial \tau_{jk}}{\partial x_1} \Delta\epsilon_{jk} dV \qquad (II.5)$$

where we have now taken the limit of the volume integral.

It has been shown in [15] that $(\Delta T_1)_c$ has the physical meaning*

$$(\Delta T_1)_c = -\left(\frac{\Delta U_2-\Delta U_1}{dc_1}\right) \qquad (II.6)$$

where ΔU_2 and ΔU_1 are the incremental potential energies for two cracked bodies which are indentical in loading history and geometry except that the second body has an incrementally longer crack by the amount dc_1. In creep applications, it is convenient to define the quantity

$$(\dot{T}_1)_c \equiv \underset{\Delta t \to 0}{\mathrm{Lt}} \frac{(\Delta T_1)_c}{\Delta t} \approx \frac{(\Delta T_1)_c}{\Delta t} \qquad (II.7)$$

where Δt is the time increment. Comparing (II.7) and (II.6) it can be seen that $(\dot{T}_1)_c$ has the physical meaning which is commonly attributed to C_1^*, i.e.

$$(\dot{T}_1)_c = -\frac{d\dot{U}}{dc_1} \qquad (II.8)$$

We now state a generalized definition for the C* parameter which has been derived in [16].

---

*The sign convention for ΔU_1 and ΔU_2 is reversed from that of [15,16] to reflect the conventional definition of potential energy.

$$C_i^* \equiv \underset{\epsilon\to 0}{\mathrm{Lt}} \int_{\Gamma_\epsilon} [n_i W^* - n_j \tau_{jk} \frac{\partial \dot{u}_k}{\partial x_i}] dS$$

$$= \int_{\Gamma_{234}} [n_i W^* - n_j \tau_{jk} \frac{\partial \dot{u}_k}{\partial x_i}] dS \tag{II.9}$$

$$+ \underset{\epsilon\to 0}{\mathrm{Lt}} \left\{ \int_{V-V_\epsilon} \rho (a_k - f_k) \frac{\partial \dot{u}_k}{\partial x_i} dV + \int_{\Gamma_{12}} n_i W^* dS + \int_{\Gamma_{45}} n_i W^* dS \right.$$

$$\left. - \int_{S_t} \bar{t}_k \frac{\partial \dot{u}_k}{\partial x_i} dS - \int_{S_e} n_j \tau_{jk} \frac{\partial \dot{\bar{u}}_k}{\partial x_i} dS \right\}$$

Based on the same simplifying conditions used in obtaining (II.5) we have

$$C_1^* = \int_{\Gamma_{234}} [n_1 W^* - n_j \tau_{jk} \frac{\partial \dot{u}_k}{\partial x_1}] dS \tag{II.10}$$

where it is seen that the volume integral no longer is present.

The quantity W* which appears in (II.9) and (II.10) is usually defined as

$$W^* = \int_0^{\dot{\epsilon}_{ij}} \tau_{ij} d\dot{\epsilon}_{ij} \tag{II.11}$$

Using the steady-state case of (II.1) and the associated incompressibility condition, the following more useful expressions can be derived [16]:

$$W^* = \frac{n}{1+n} \left(\frac{1}{\gamma}\right)^{1/n} (\dot{\bar{\epsilon}})^{\frac{1+n}{n}} \tag{II.12}$$

$$W^* = \frac{n}{1+n} \gamma (\bar{\sigma})^{1+n} \tag{II.13}$$

As noted previously, C_1^* is often stated to have the energy interpretation which was given for $(\dot{T}_1)_c$ in (II.8). It has been shown in [16] that this incorrect. The relationship of the steady-state value of $(\dot{T}_1)_c$ (i.e. $(\dot{T}_1)_{css}$) and C_1^* is given in [16] as:

$$(\dot{T}_1)_{css} = C_1^* + \left(\frac{\gamma}{n+1}\right) \underset{\epsilon\to 0}{\mathrm{Lt}} \int_{\Gamma_\epsilon} n_1 (\bar{\sigma})^{n+1} dS \tag{II.14}$$

Approximate numerical evaluation of (II.14) in [16] has shown that $(\dot{T}_1)_{css}$ and C_1^* agree to within 2% for plane strain and differ by as much as 14% for plane stress.

From the above discussion it is clear that $\underline{C}^*$ and $(\dot{\underline{T}})_c$ are not equivalent quantities under any condition despite their being derivable from the same conservation law. The quantity $(\dot{\underline{T}})_c$ follows more directly from the conservation law and is the more general quantity not only in that it is applicable to non-steady as well as steady-state creep but also in that it is applicable to constitutive laws which are more general than (II.1) [15]. The quantity $\underline{C}^*$ relies on the special property of (II.1) which allows the existance of a potential W* for the deviatoric stresses, τ'_{ij}. Furthermore, since W* does not have a physical meaning whereas $\dot{W}$ has the meaning of rate of stress-working density, it is understandable that $(\dot{\underline{T}})_c$ has an energy interpretation whereas $\underline{C}^*$ does not. In light of this conclusion, it seems more appropriate to refer to experimental measurements of "$-\frac{d\dot{U}}{da}$" as measurements of $(\dot{T}_1)_c$ as opposed to measurements of C_1^* or $\dot{J}_1$ etc.

Finite Element Equations:

The following summarizes the finite element model. For a more complete description see [16]. The model is based on the principle of virtual work:

$$\int_V \tau_{ij}\delta\epsilon_{ij}dV - \int_{S_t} \bar{t}_i\delta u_i dS = 0 \qquad \text{(II.15)}$$

By substituting the following incremental stress-strain relation

$$\{\tau\}_I = \{\tau\}_{I-1} + [E]\{\Delta\epsilon\}_I - [E]\{\Delta\epsilon^c\}_I \qquad \text{(II.16)}$$

into (15) and applying customary procedures we have the final equation:

$$[K]\{\Delta Q\}_I = \{T\}_I + \{S_c\}_I - \{R\}_{I-1} \qquad \text{(II.17)}$$

In the above, $\{(\ )\}_I$ indicates the quantity at the end of the Ith increment and $\{\Delta(\ )\}_I$ the increment in the quantity for the Ith increment. The incremental node displacements are denoted $\{\Delta Q\}_I$. The remaining terms of (II.17) as follows:

$$[K] = \sum_e \int_{V_e} [B]^T[E][B]dV \tag{II.18}$$

$$\{T\}_I = \sum_e \int_{S_{t_e}} [N]^T\{\bar{t}\}_I dS \tag{II.19}$$

$$\{S_c\}_I = \sum_e \int_{V_e} [B]^T[E]\{\Delta\epsilon^c\}_I dV \tag{II.20}$$

$$\{R\}_{I-1} = \sum_e \int_{V_e} [B]^T\{\tau\}_{I-1} dV \tag{II.21}$$

The form of (II.17) makes this an initial strain formulation. It can be seen that [K] is the elastic stiffness matrix and remains unchanged throughout the time incrementing process. The quantities $\{\Delta\epsilon^c\}_I$ in (20) are predicted prior to the solution of (II.17) using (II.1) and $\{\tau\}_{I-1}$. Having sovled (II.17), and thus obtained $\{\Delta\epsilon\}_I$, the actual values of $\{\Delta\epsilon^c\}_I$ and $\{\Delta\tau\}_I$ are obtained by subdividing the time step and performing an Eulerian integration based on subincrements of $\{\Delta\epsilon\}_I$. As a result of this integration procedure, better adherence to the postulated constitutive law (II.1) is achieved but at the price of introducing some disequilibrium (i.e. $\{R\}_I \neq \{T\}_I$). This disequilibrium is corrected, however, in the next time step as a consequence of $\{R\}_{I-1}$ appearing in (II.17).

The time step size for the calculations is automatically regulated based on two criteria. The first criteria is the maximum error in the predicted creep strain increments used in solving (II.17) as compared to the creep strain increments from the subsequent integration procedure. The second criteria is the maximum creep strain increment compared to the total elastic strain. In the present study, the criterion for maximum error in predicted creep strain is 20% and the criterion for maximum creep strain increment is 100%. For problems which have been considered, it appears that the above model and criteria give accurate transient solutions and converged steady-state solutions with time step size comparable to those used with more expensive tangent stiffness methods.

Verification of Model:

A compact specimen has been chosen for verifying the model. The particular geometry and materials were chosen to coincide with those used by Ehlers and Riedel [17] and are illustrated in Fig. 13 along with the two finite element meshes used in the verification. Both meshes consist entirely of eight-noded isoparametric elements, assume plane strain conditions and use collapsed (i.e. triangular) elements at the crack-tip. For the 102 element model these crack-tip elements are given a singular strain field $(r^{-1/2})$ by shifting the appropriate midside nodes to their quarter-points. The 300 element model uses a non-singular crack-tip.

The elastic J_1 for the 300 and 102 element meshes are 24.1 and 24.3 N/mm, respectively and agree with the value 24.2 N/mm from Srawley [18] to well within 1%. The steady-state (t=600hr) values of C_1^* for the 300 and 102 element meshes are 131 and 130 N/m·hr, respectively, and agree well with 134 N/m·hr from Shih and Kumar [19] and 137 N/m.hr (t 300hr) from Ehlers and Riedel [17]. Based on these results it is concluded that the numerical procedure in general and the quarter-point crack-tip elements in particular, are accurate and efficient tools for creep fracture analysis.

Calculations of $(\dot{T}_1)_c$ and $(\dot{T}_1)_c^\delta$:

Now we consider calculations of $(\dot{T}_1)_c$ (i.e. $(\Delta T_1)_c/\Delta t$). The 300 element mesh results for $(\dot{T}_1)_c$, as computed from (II.5), are shown in Fig. 14 as the solid curve. This curve shows the time dependence of $(\dot{T}_1)_c$ during the non-steady portion of the creep calculation. The steady-state value of $(\dot{T}_1)_c$ is 130 N/m·hr and thus is in agreement with the previously mentioned relationship between $(\dot{T}_1)_{css}$ and C_1^*. In [16] it was found that the evaluation of (II.5) using the 102 element mesh gave values of $(\dot{T}_1)_c$ which were generally in poor agreement with those of the 300 element mesh. The volume integral of (II.5) was determined to be the cause of this behavior and it was supposed that the origin of the problem was the use of the $r^{-1/2}$ strain singularity as opposed to the HRR type singularity (i.e. $r^{-n/(1+n)}$). However, several calculations with special conforming elements which impose the HRR type radial dependence of strain [20], have shown that this is not the case.

It now seems that the difficulty experienced in computing $(\dot{T}_1)_c$ when using singular crack-tip elements is related to the existence argument for the limit of the volume integral in (II.3). For the case when the asymptotic field has singular radial dependence but does not identically satisfy the following condition on angular behavior,

$$\underset{\epsilon\to 0}{\mathrm{Lt}} \int_{-\pi}^{\pi} \frac{\partial \tau_{ij}(\epsilon,\theta)}{\partial x_1} \Delta\epsilon_{ij}(\epsilon,\theta)d\theta = 0 \qquad \text{(II.22)}$$

the subject limit in (II.3) does not exist (as discussed in Appendix A of [16]). The condition (II.22) need not be satisfied exactly if one does not ahve a singular radial dependence as is demonstrated by the results from the 300 element mesh.

The efficiency, simplicity and general accuracy of the quarter-point element procedure makes it a very attractive alternative to the use of very refined nonsingular meshes or the derivation of singular crack-tip elements which satisfy (II.22) a priori. Therefore, a practical solution to this problem is sought. As noted above, the difficulty is associated with the volume integral over the singular elements. Therefore, calculations were made in which the volume integral over the crack-tip elements was omitted. The resulting quantity, which we call $(\dot{T}_1)_c^\delta$, can be written

$$(\dot{T}_1)_c^\delta = \int_{\Gamma_{234}} [n_1 \Delta W - n_j(\tau_{jk}+\Delta\tau_{jk}) \frac{\partial \Delta u_k}{\partial x_1}] dS - \int_{V-V_\delta} \frac{\partial \tau_{jk}}{\partial x_1} \Delta\epsilon_{jk} dV \qquad \text{(II.23)}$$

where V_δ consists of the singular crack-tip elements. The dashed curve of Fig. 14 is $(\dot{T}_1)_c^\delta$ from the 102 element mesh. It can be seen that $(\dot{T}_1)_c^\delta$ coincides with the solid curve for times after about 30 hours. For this mesh and problem it can therefore be said that $(\dot{T}_1)_c^\delta$ is a valid path-independent, crack-tip parameter for times after 30 hours and for values of $(\dot{T}_1)_c$ beginning at approximately 1.6 of the steady-state value. The steady-state parameter C_1^* is still significantly path-dependent at 30 hours.

For the 102 element mesh, the crack-tip elements are 5% of the ligament size. We therefore assign δ a value of 0.05. A quantity similar to $(\dot{T}_1)_c^\delta$ was computed using the 300 element mesh. In this case, a semi-circular region of radius approximately 3% of the ligament was omitted from the evaluation of the volume integral of (II.5). This result which we deonte $(\dot{T}_1)_c^\epsilon$ with ϵ=3% is also shown in Fig. 14. This curve seems to indicate that the validity of $(\dot{T}_1)_c^\delta$ can be expanded to earlier times with rather moderate reductions in the crack-tip, quarter-point element size. For example, the results of Fig. 14 indicate that a δ of 3% of the ligament would result in $(\dot{T}_1)_c^\delta$ being valid as early as seven hours and for $(\dot{T}_1)_c$ as large as 4.3 its steady-state value.

Creep Crack Growth in a Strip:

We now consider the problem of a finite height (2h) infinitely wide strip, with a semi-infinite crack. Loading consists of uniformly applied displacement rates ($\dot{\delta}$) at the top and bottom edges ($y=\pm h$) such that Mode I behavior results. This problem has been chosen for two reasons. First, since the strip is infinitely wide and the boundary conditions do not change with time, the propagating crack-tip fields can be expected to reach a "convecting steady-state" creep condition. Here we use the phrase "convecting steady-state" to mean that the field remains unchanged in time with respect to a coordinate system which is centered at and moving with the crack-tip. This terminology is used so as not to confuse this condition with the usual steady-state creep condition in which material stress rates are zero.

The second reason for choosing this problem is that C_1^* can be evaluated analytically for the special case of steady-state creep (stationary crack). The analytical evaluation of (II.10) follows easily if one chooses a rectangular contour in which the horizontal portions coincide with the top and bottom edges of the strip (i.e. $y=\pm h$) and the vertical portions are at $x=\pm\infty$. In such a contour one finds only the vertical portion at $x=+\infty$ is non-zero and therefore

$$C_1^* = 2hW_\infty^* \qquad \text{(II.24)}$$

For the corresponding elastic problem with applied displacement δ, one finds a similar relation.

$$J_1 = 2hW_\infty \qquad \text{(II.25)}$$

It has been noted that $(\dot{T}_1)_{css}$ and C_1^* are related and therefore it is possible to obtain $(\dot{T}_1)_{css}$ from (II.14) and (II.24). The direct evaluation of $(\dot{T}_1)_c$ in terms of either its integral representation (II.5) or its energy representation II.6) requires knowledge of the stresses in the region of the strip adjacent to the crack-tip and therefore is not a trivial task.

The material properties used in this problem are representative of 304 stainless steel at 650°C. These material properties and the finite element

Table 1. Summary of Analysis Parameters for Creep Crack Growth

in the Plane Strain Strip of Fig. 15

Analytical Results					Computed Results		$\frac{da}{dt}$ from (6.4) (mm/hr)	
C^*_1 (N/mm·hr)	remote τ_{yy} (MPa)	$\dot{\delta}$ (mm/hr)	δ (elastic) (mm)	J_1 (N/mm)	C^*_1 (N/mm·hr)	J_1 (N/mm)	average	upper bound
0.05	83	3.44×10^{-4}	5.04×10^{-2}	4.18	4.99×10^{-2}	4.19	1.00×10^{-4}	5.00×10^{-4}
5.0	148	1.94×10^{-2}	8.95×10^{-2}	13.2	4.99	13.2	2.22×10^{-2}	1.11×10^{-1}
50	197	1.45×10^{-1}	1.19×10^{-1}	23.5	49.8	23.5	3.30×10^{-1}	1.65

discretization are given in Fig. (15). Note that collapsed, eight-noded, quarter-point elements are used at the crack-tip.

The mesh for this problem may at first appear rather coarse; however, elastic and steady-state creep solutions obtained with this mesh are sufficiently accurate to justify its use for the study at hand. The comparison of computed elastic J_1 values and steady-state C_1^* values with their analytic values is given in Table 1.

The first step in this numerical study is to select three values of C_1^* which span the range of values reported in the literature for 304 stainless steel at 650°C.† The values which have been chosen are 0.05, 5.0 and 50.0 N/mm·hr. Having these values, the remote ($x=\infty$) steady-state τ_{yy} are determined as well as the edge displacement which results in the same remote elastic τ_{yy}. These displacements are applied to the model elastically at $t=0$. Next, the steady-state edge displacement rates are determined analytically. Using the elastic solution as an initial state, the displacement rate, $\dot{\delta}$, is applied until the model reaches steady-state.

The next step in this study involves the selection of upper bound crack velocities for the three chosen values of C_1^*. The following formula is based on the experimental data reported in [13,14] and represents data from center-crack, double-edge-crack, compact, and round bar specimen types.

$$\frac{da}{dt} = \alpha[C_1^*]^{1.173} \tag{II.26}$$

$$\text{where } \alpha = \begin{cases} 1.68 \times 10^{-2} & \text{(upper bound)} \\ 3.36 \times 10^{-3} & \text{(average)} \end{cases}$$

---

†The use of C_1^* rather than $(\dot{T}_1)_c$ is due to the existence of the analytical expression (24) and is justified by the numerical similarity to $(\dot{T}_1)_c$ for plane strain conditions.

Having reached steady-state, the crack is propagated at the upper bound velocity of (II.26) until it is determined that a convecting steady-state has been reached.

The crack growth simulation is accomplished through a combination of mesh shifting and periodic remeshing as illustrated in Fig. (16). The region A represents the quarter-point elements which remain centered about the crack-tip. The B type elements are standard eight-noded isoparametric elements which distort during mesh shifting so as to keep the region A centered at the crack-tip. The procedure is to shift the region A (and thus the crack-tip) by shifting appropriate nodes of the region A and type B elements. This shifting is done without altering element connectivity. Eventually the type B elements become overly distorted at which time the element connectivities are redefined in the vicinity of the crack-tip so that additional shifting is possible.

Each occurance of shifting or remeshing requires that shifted nodes have their displacements interpolated and that shifted elements have their 2x2 Gauss point stresses interpolated. The displacement interpolation is by the usual isoparametric shape functions. The stress interpolation uses linear, two-dimensional Lagrangian polynomials in element local coordinates. In the following calculations, the nominal size of the crack growth increments is 0.4 mm or 2% of the crack-tip element width. For the highest velocity case (C_1^*=50 N/mm·hr), this results in crack growth at approximately every fifth solution step.

Results for a Plane Strain Strip:

The results of the plane strain strip calculation with C_1^*=50 N/mm·hr and $\frac{da}{dt}$ =1.65 mm/hr are given in Fig. 17. The values of $(\dot{T}_1)_c^\delta$ and C_1^* are given for the portion of the calculation prior to steady-state as well as during the crack propagation portion. The band represents the range of values obtained from the four contours illustrated in Fig. 15. Both $(\dot{T}_1)_c^\delta$ and C_1^* converge to the 50 N/mm·hr value at steady-state. During the crack propagation, it is seen that $(\dot{T}_1)_c^\delta$ and C_1^* do not depart significantly from their steady-state value. This means that this combination of loading and crack-speed results in the crack-tip fields being essentially at steady-state conditions. This in turn means that both $(\dot{T}_1)_c^\delta$ (or $(\dot{T}_1)_c$) and C_1^* are valid crack-tip field parameters during crack growth.

A closer view of the crack propagation portion of these curves is given in Fig. 18. The dashed curves bracketing the initial portion of the solid curves represent the degree of path-independence and continue to be representative of the path-independence observed during the crack propagation steps. For both $(\dot{T}_1)_c^\delta$ and C_1^*, it is seen that the strip has essentially returned to its steady-state condition prior to each crack growth increment. It is thought that the larger departure of $(\dot{T}_1)_c^\delta$ from steady-state (as compared to C_1^*) is more representative of the non-steadiness of the crack-tip field since the validity of C_1^* in general and the numerical evaluation of W^* (II.13) in particular, are based on the existence of steady-state conditions.

The effect of remeshing is seen at approximately eight hours. The first two steps after the remeshing were found to result in rather erratic contour integral values and are not indicated in these figures. The equilibrium correction feature of the present model and the automatic time step regulation procedure both act to quickly restore equilibrium at the crack-tip.

The propagation portion of the calculation with C_1^*=5 N/mm·hr and $\frac{da}{dt}$ =0.111 mm/hr is given in Fig. 19. Here again it is seen that both $(\dot{T}_1)_c^\delta$ and C_1^* have converged to the analytical value of C_1^* (to within two percent, which is also about the degree of path-independence). Comparing these results with those in Fig.18 for the higher C_1^* and crack speed it is seen that steady-state creep conditions were not reached until 12 hours as opposed to approximately two hours in previous cases. Also, the return to the steady-state value after mesh shifting takes more time (two hours compared to 0.25 hours). However, when compared to the time between crack growth steps (both use·0.4 mm) it is seen that the lower velocity case returns to steady-state well before the next growth step occurs. This result indicates that lower load levels and crack speeds are inherently closer to steady-state conditions. While this behavior seems intuitively correct, it should be kept in mind that these results depend on the empirical formula (II.26) which is valid only for 304 stainless steel. It remains to be seen if similar behavior occurs in other materials.

A calculation has also been done for the case of $C_1^*=0.05$ N/mm·hr. As a result of the large number of solution steps between crack growth steps, when using the maximum velocity of 5×10^{-4} mm/hr, the calculations used a higher velocity (5×10^{-3} mm/hr). Even at this unrealistically high velocity (for this level of loading), the behavior is more steady-state-like than the case of $C_1^*=5.0$ N/mm.hr described above.

Creep Crack Growth in Double-Edge-Crack Specimens:

The purpose of considering this problem is to apply the model to a problem for which experimental data exists. While much experimental data has been reported in the literature, most authors do not include sufficient information to allow a numerical simulation of their experiments. The current problem is based on the experiments of Koterazawa and Iwatwa [21]. The primary reasons for selecting this work for study are the crack length versus time histories were given and that the experiments were performed on 304 stainless steel for which high temperature elastic and creep properties were already available.

The geometry of the experimental specimens is given in Fig. 20. The finite element mesh for the calculations is shown in Fig. 21 with contour integral paths being indicated by dashed lines. It can be seen that the mesh takes advantage of the two planes of symmetry for the specimen and does not model the 60° notch. The initial crack length indicated in Fig. 21 corresponds to the notch depth in the specimen. All calculations for this specimen assume plane stress conditions and use the material properties given in Fig. 15. Elastic J_1 results for two crack lengths are compared in Table 2 with those (based on formulas for K_I) from [22] and are seen to be in good agreement.

The material properties are those of 304 stainless steel at 650°C and are assumed to be the same as those used in the strip analyses. (See Fig. 15). Calculations have been made for remote applied stresses of 157 and 176 MPa. The experimental crack growth histories for these two stress levels are reproduced from [21] in Fig. 22. It is seen from these curves that the first two-thirds of the specimen lives are characterized by crack velocities of less than 0.01 mm/hr compared to nearly 0.5 mm/hr as rupture is approached.

The primary purpose of the following calculations is to verify the conclusions which were reached in the previously described strip calculations; that is, that the crack-tip fields are essentially creep-steady fields even for the most rapid creep crack velocities. These calculations will be a valid check because the input to the calculations is only the remote applied stress and the measured crack velocity history, and does not in any way depend on experimental determination of C_1^* or $(\dot{T}_1)_c$ as did the strip calculations. In fact, Koterazawa and Iwata do not report such measurements in [21].

Analysis of Initial, Low Velocity Crack Growth:

This section describes the simulation of the initial portion of the crack velocity histories given in Fig. 22. In all of these calculations, the entire load is applied elastically at $t = 0$ and held constant throughout the subsequent creep solution steps. The convergence of $(\dot{T}_1)_c$ and C_1^* to their steady-state values is shown in Fig. 23, with the dashed lines in the C_1^* plots denoting the degree of path-independentce. It is seen that steady-state conditions are reached between a half and one hour after the load is applied. (Table 2 summarizes the computational aspects of this portion of the calculation.) Therefore, it is seen by refering to Fig. 22 that crack growth does not begin in the two specimens until well after steady-state conditions are reached. Since the current calculations assume small displacements and infinitesimal strains, and since only the strain and displacement magnitudes depend on time once steady-state is reached, there is no reason to continue the numerical calculations to the crack initiation times indicated by the experimental results. Therefore, the initial crack propagation is simulated at times after steady-state conditions are reached but much earlier indicated by the experiments.

The crack growth simulation results are shown in Fig. 23. The crack increment size for this study was approximately 0.01 mm which is nominally 2.4 percent of the crack-tip element size. It can be seen that only one mesh shift (i.e., crack growth step) was modeled. It is clear from this figure that the time it takes for the specimen to return to steady-state is significantly less than the time to the next crack growth increment (indicated by dashed lines). Therefore, the initial portion of the crack growth histories of Fig. 22 are clearly occurring under essentially steady-state conditions and thus C_1^* as well as $(\dot{T}_1)_c$ are valid crack-tip parameters. Since an increase in C_1^* results in a more rapid return to steady-state conditions, the above conclusion will remain valid for the initial constant velocity portions of the curves of Fig. 22.

When crack growth occurs so slowly that the crack-tip is essentially at steady-state, the crack-tip field does not depend on the history of the specimen. Therefore, assuming steady-state conditions continue to exist, it is possible to skip to the final stages of crack growth without modeling the intermediate crack growth. If it is found that crack growth is still slow enough for steady-state conditions to exist, then it seems reasonable to expect that the behavior at intermediate crack lengths is also of a steady-state type. The following describes the results of this procedure when applied to the two double-edge-crack specimens.

Analysis of Final Stage of Crack Growth:

To analyze the final stage of crack growth, the crack length is increased to 2.75 mm and the process of applying the load elastically and creeping to steady-state is repeated. Table 2 summarizes the computational aspects of this process. The convergence of $(\dot{T}_1)_c^{\delta}$ and C_1^* is their steady-state values is shown in Fig. 24. Having reached steady-state, the cracks are grown at the rate suggested by the last portion of the crack histories (Fig. 22)as shown in Fig. 24 . The significant increase in the frequency of mesh shifting (compared to that in Fig. 23 due to the velocity increase makes the details of the curve difficult to distinguish in this figure. However, the time step size is such that six or seven steps occur between each crack growth increment. Unlike the strip problem, the values of $(\dot{T}_1)_c^{\delta}$ and C_1^* are clearly increasing during this crack propagation process.

It is necessary to determine whether this increase in the crack-tip parameters is due to the crack-tip no longer being at steady-state conditions or whether it is due to the crack-tip no longer being at steady-state conditions or whether it is due to the incraese in crack length. This is accomplished by continuing the calculation without further crack extension. If the value of the parameters do not change significantly with time, this means the increase was largely due to the crack length increase and that crack growth is still occuring under essentially steady-state conditions. Examination of the final portions of the curves of Fig. 24 shows that this is the case.

Table 2. Computational Aspects of the Elastic and Non-Steady Creep Portion of the Double-Edge-Crack Calculations

		Elastic Solution			Creep Solution		
applied stress (MPa)	crack length (mm)	J_1 (N/mm)	difference from [2] (%)	CP time* (sec)	Δt (hr) initial/final	steps to steady-state†	total CP time (sec)
157	1.75	1.12	(-2.1)	38	$8 \cdot 10^{-8}/1.9 \cdot 10^{-2}$	90	795
176	1.75	1.40	(-2.6)	38	$8 \cdot 10^{-8}/9.5 \cdot 10^{-3}$	100	880
157	2.75	1.79	(-3.3)	38	$4 \cdot 10^{-8}/8.6 \cdot 10^{-3}$	211	1820
176	2.75	2.25	(-3.2)	38	$2 \cdot 10^{-8}/4.4 \cdot 10^{-3}$	205	1770

*Control Data CYBER 74

†Solutions are stopped at times indicated in Figs. 5.19 and 5.20

Based on this analysis; it appears that the conclusions reached as a result of the strip calculations are still valid. Since, (i) the strip analyses are much less expensive than this analysis of the double-edge-crack geometry, (ii) the steady-state C_1^* for the strip is easily obtained analytically and (iii) the crack-tip parameters do not depend on crack length for the strip geometry, it seems that similar studies for other materials and/or other temperatures could most effectively be accomplished through the use of the strip geometry. The need for such studies follows from the vast simplification of fracture analysis and prediction which results if crack growth occurs under steady-state conditions. More will be said about this point in the conclusions.

Summary and Conclusions:

It has been noted that despite the fact that C_1^* characterizes the crack-tip field under steady-state creep conditions, it does not have an energy or energy rate interpretation. A related path-independence integral parameter $(\dot{T}_1)_c$, however, does have the energy rate interpretation commonly attributed to C_1^*. The derivation of $(\dot{T}_1)_c$ does not rely on the existence of steady-state creep conditions and thus is a valid crack-tip parameter for non-steady creep conditions as well as for steady-state creep.

An initial strain finite element approach provides for improved adherence to postulated constitutive behavior and for equilibrium correction has been summarized. The accuracy and efficiency of this model with eight-node isoparametric elements and the quarter-point crack-tip element approach have been verified through several calculations for a compact specimen geometry and a strip geometry. Also, a method of simulating crack growth through shifting of the quarter-point singularity elements and periodic remeshing has been described and demonstrated.

A creep crack growth simulation for 304 stainless steel has shown that for realistic load levels and corresponding crack speeds the crack-tip field is essentially at a steady-state creep condition. This means that for this material the propagating crack-tip field is largely unaffected by the history of crack-growth or the history of loading. This feature can greatly reduce the analysis requried for predicting creep crack growth behavior in a component as can be seen from the following suggested methodology.

We assume that the crack propagation speed $\frac{da}{dt}$ is related to $(\dot{T}_1)_{css}$ (i.e., $-\frac{d\dot{U}}{dt}$) through the poer law suggested by experimental data [13,14]

$$\frac{da}{dt} = \alpha[(\dot{T}_1)_{css}]^{\beta} \tag{II.27}$$

Next we determine (eg. by steady-state creep finite element analysis) $(\dot{T}_1)_{css}$ as a function of crack length. Because of the assumed steady-state crack-tip behavior, this can be accomplished by considering several discrete crack lengths and then fitting a curve. No crack growth simulation procedures are necessary. Combining (II.27) with this result provides the followng relationship between time and crack length

$$t = \int_{a_o}^{a(t)} \frac{[(\dot{T}_1)_{css}]^{-\beta}}{\alpha}\, da + t_i \tag{II.28}$$

where a_o is the initial crack length and t_i is the time when crack growth initiates. The only unknown quantity in (II.28) is the initiation time t_i.

Vitek [23] has simulated several experiments (compact and double-edge-crack specimens) on two CrMoV steels using a dislocation model and has concluded that COD correlated well with the initiation of crack growth in these experiments. If the same conclusion is valid for 304 stainless steel, then one can presumably predict t_i based on a transient finite element analysis of the initial flawed configuration and a critical value of COD. If initiation occurs long after steady-state conditions are reached, it is then reasonable to estimate t_i using the rate of COD obtained from a steady-state finite element solution. At this time, the validity of (II.28) and of the critical COD concept has not been investigated by the authors.

Acknowledgements:

The final support for this work provided through NASA grant NAG-3-38 from NASA-Lewis Research Center to Georgia Institute of Technology is gratefully acknowledged. The timely encouragement of Drs. M. Hischberg, B. Gross, and J. Srawley of NASA-Lewis Research Center is sincerely appreciated. Thanks are expressed to Ms. M. Eiteman for her careful assistance in the preparation of this manuscript.

References:

[1] Pian, T.H.H., "Derivation of Element Stiffness Matrices by Assumed Stress Distributions", AIAA Journal, Vol. 2, No. 7, pp. 1333-1336, 1964.

[2] de Veubeke, B.F., A New Variational Principle for Finite Elastic Deformations", International Journal of Engineering Science, Vol. 10, pp. 745-763, 1972.

[3] Atluri, S.N., "On Some New General and Complementary Energy Theorems for the Rate Problems of Finite Strain, Classical Elasto-Plasticity", Journal of Structural Mechanics, Vol. 8, No. 1, 1980, pp. 61-92.

[4] Atluri, S.N. and Murakawa, H., "New General and Complementary Energy Theorems, Finite Strain, Rate Sensitive Inelasticity and Finite Elements: Some Computational Studies," in Nonlinear Finite Element Analysis in Structural Mechanics, Wunderlich, W., Stein, E., and Bathe, K.-J., Editors, Springer-Verlag, 1981.

[5] Murakawa, H., "Incremental Hybrid Finite Element Methods for Finite Deformation Problems (with Special Emphasis on the Complementary Energy Principle)", Ph.D. Dissertation, Georgia Inst. of Technology, Aug., 1978.

[6] Reed, K.W., "Analysis of Large Quasistatic Deformations of Inelastic Solids by a New Stress-Based Finite Element Method", Ph.D. Dissertation, Center for the Advancement of Computational Mechanics, Georgia Institute of Technology, April, 1982.

[7] Cormeau, I., "Numerical Stability in Quasistatic Elasto-Viscoplasticity", Int. J. Numer. Methds. in Eng., Vol. 9, 1975, pp. 109-127.

[8] Argyris, J.H., Vaz, L.E. and Willam, K.J., "Improved Solution Methods for Inelastic Rate Problems", Computer Methods in Applied Mechanics and Engineering, Vol. 16, 1978, pp. 231-277.

[9] Kanchi, M.B., Zienkiewicz, O.C. and Owen, R.J., "The Visco-Plastic Approach to Problems of Plasticity and Creep Involving Geometric Nonlinear Effects", Int. J. Numer. Meths. Eng., Vol. 12, 1978, pp. 169-181.

[10] Burke, M.A. and Nix, W.D., "A Numerical Analysis of Void Growth in Tension Creep", Int. J. Solids Structures, Vol. 15, 1979, pp. 55-71.

[11] Fu, L.S., "Creep Crack Growth in Technical Alloys at Elevated Temperature-a Review", Engng. Fracture Mech., Vol. 13, 1980, pp. 307-330.

[12] Landes, J.D. and Begley, J.A., "A Fracture Mechanics Approach to Creep Crack Growth", Mechanics of Crack Growth, ASTM STP 590, 1976, pp. 128-148.

[13] Ohji, J., Ogura, K. and Kubo, S., "The Application of Modified J-Integral to Creep Crack Growth in Austenitic Stainless Steel and Cr-Mo-V Steel", Engng. Aspects of Creep, Proc. Conf. at Univ. Sheffield, I. Mech. E., 1980, pp. 9-16.

[14] Koterazawa, R., Mori, T., "Applicability of Fracture Mechanics Parameters to Crack Propagation Under Creep Conditions", J. Engng. Materials and Technology, Vol. 99, Series H, No. 4, 1977, pp. 298-305.

[15] Atluri, S.N., "Path-Independent Integrals in Finite Elasticity and In-Elasticity, with Body Forces, Inertia, and Arbitrary Crack-Face Conditions", Report No. GIT-CACM-SNA-81-8, Georgia Institute of Technology, March, 1981, also Engng. Fracture Mech., Vol. 13, No. 2, 1982.

[16] Stonesifer, R.B. and Atluri, S.N., "On a Study of the $(\Delta \underline{T})_c$ and C* Integrals for Fracture Analysis Under Non-Steady Creep", Report No. GIT-CACM-SNA-81-21, Georgia Institute of Technology, July 1981, also Engng. Fracture Mechanics (in press).

[17] Ehlers, R. and Riedel, H., "A Finite Element Analysis of Creep Deformation in a Specimen Containing a Macroscopic Crack", Advances in Fracture Research Vol. 2, Francois, D., (Ed.), Fifth Intl. Conf. on Fracture, Ca-nes, 1981, 691-698.

[18] Srawley, J.F., "Wide Range Stress Intensity Factor Expressions for ASTM E399 Standard Fracture Toughness Specimens", Intl. J. Fracture, 12, 1976, pp. 475-476.

[19] Shih, C.F. and Kumar, V., "Estimation Technique for the Prediction of Elastic-Plastic Fracture of Structural Components of Nuclear Systems", Contract RP 1237-1, First Semiannual Report for Electric Power Research Institute, General Electric Co., Report, 1979.

[20] Stonesifer, R.B., <u>Fast Brittle Fracture and Creep Crack Growth: Moving Singularity Finite Element Analysis</u>, Ph.D. Dissertation, Dept. of Civil Engineering, Georgia Institute of Technology, 1981.

[21] Koterazawa, R. and Iwata, Y., "Fracture Mechanics and Fractography of Creep and Fatigue Crack Propagation at Elevated Temperature", J. of Engng. Mat. and Technology, 98, 1976, pp. 296-304.

[22] Tada, H., Paris, P.C. and Irwin, G.R., The Stress Analysis of Cracks Handbook, Del Research Corp., Hellertown, PA, 1973.

[23] Vitek, V., "A Theory of the Initiation of Creep Crack Growth", Int. J. of Fracture, Vol. 13, No. 1, 1977, pp. 39-50.

APPENDIX A

Plane Strain:

The deformation studied in the example accompanying Part I of this report is plane strain in the character. Just as for formulations using ordinary stresses, a number of the components of the velocity, spin, and stress rate vanish if a Cartesian coordiante system is chosen with one axis normal to the plane of deformation. We have chosen the x^2 coordinate line to be normal to the plane of deformation, so that the velocity, spin, stress rate, and stress are of the forms

$$\underline{v} = v^1\underline{e}_1 + v^3\underline{e}_3$$

$$\underset{\sim}{\omega} = \omega^{13}\underline{e}_1\underline{e}_3 + \omega^{31}\underline{e}_3\underline{e}_1$$

$$\begin{aligned}\underset{\sim}{\dot{t}} = {} & \dot{t}^{11}\underline{e}_1\underline{e}_1 + \dot{t}^{13}\underline{e}_1\underline{e}_3 + \dot{t}^{22}\underline{e}_2\underline{e}_2 \\ & + \dot{t}^{31}\underline{e}_3\underline{e}_1 + \dot{t}^{13}\underline{e}_3\underline{e}_3\end{aligned}$$

$$\begin{aligned}\underset{\sim}{\tau} = {} & \tau^{11}\underline{e}_1\underline{e}_1 + \tau^{13}\underline{e}_1\underline{e}_3 + \tau^{22}\underline{e}_2\underline{e}_2 \\ & + \tau^{31}\underline{e}_3\underline{e}_1 + \tau^{33}\underline{e}_3\underline{e}_3\end{aligned}$$

None of the components depends upon x^2. The velocity is represented on each element as

$$\underline{v} = \sum_{i=1}^{NQ} N_i q^i$$

The shape functions $\underline{N}_i$ are described below. Similarly the spin and stress rate are represented as

$$\underset{\sim}{\omega} = \sum_{i=1}^{NW} \underset{\sim}{QW}_i \alpha^i ; \quad \dot{\underset{\sim}{t}} = \sum_{i=1}^{NT} \underset{\sim}{QT}_i \beta^i$$

We note that this approach requries minimal specialization in programming for the particular case of plane strain. The plane strain condition is not satisfied a priori; that is

$$\delta\varepsilon_{22} = (\underline{e}_2\underline{e}_2):\underset{\approx}{W}^{-1}:\delta\dot{\underset{\sim}{r}} \neq 0$$

for arbitrary $\delta\dot{\underset{\sim}{r}}$. Rather, $\varepsilon_{22}=0$ follows from the stationary condition (a component of 7.1):

$$\int_V [-\varepsilon_{22}(\dot{\underset{\sim}{t}},\underset{\sim}{\omega})]\delta\dot{t}^{22} dV = 0$$

In using the finite element algorithm the plane strain condition is only satisfied approximately. In practice a qulitative check for satisfaction of the plane strain condition can be made by seeing that the stress component τ^{22} and the mean stress are nearly equal. This method for checking $\tau_{22}=0$ works so long as the inelastic stretching is proportional to the stress deviator (in the constitutive equation).

SHAPE FUNCTIONS FOR VELOCITY, STRESS RATE, AND SPIN

Shape Functions for Plane Strain

$$x^i = X \qquad x^3 = z$$

VELOCITY SHAPE FUNCTIONS

$$\underline{N}_i = N_{1,i}\underline{e}_1 + N_{3,i}\underline{e}_3$$

FOUR NODED ELEMENT:

$$N_{1,i} = \begin{cases} \frac{1}{4}(1+\xi\xi_i)(1+\eta\eta_i) & i=1,2,3,4. \\ 0 & i=5,6,7,8. \end{cases}$$

$$N_{3,i} = \begin{cases} 0 & i=1,2,3,4. \\ \frac{1}{4}\,(1+\xi\xi_{i-4})(1+\eta\eta_{i-4}) & i=5,6,7,8. \end{cases}$$

$|\xi|\leq 1, \ |\eta|\leq 1,$

$\xi_1 = -1, \ \xi_2=1, \ \xi_3=1, \ \xi_4=-1$

$\eta_i = -1, \ \eta_2=-1, \ \eta_3=1, \ \eta_4=1$

SHAPE FUNCTIONS FOR SPIN:

$QW(1,3,1) = C_1$

$\underset{\sim}{QW}_i \underset{\sim}{QW}_{13,i}\underline{e}_1\underline{e}_3+QW_{31,i}\underline{e}_3\underline{e}_1$

$QW(3,1,1) = -C_1$

$QW(1,3,2)=X\ C_2$

$QW(1,3,3)=Z\ C_3$

$QW(3,1,2) = -X\ C_2$

$QW(3,1,3)=-Z\ C_3$

The constants were used to improve the condition of [H].

STRESS SHAPE FUNCTIONS:

$QT(1,1,1)=1$

$$QT_i=QT_{11,i}\underline{e}_1\underline{e}_1 + 0 + QT_{13,i}\underline{e}_1\underline{e}_3$$
$$+ 0 + QT_{22,i}\underline{e}_2\underline{e}_2 + QT_{31,i}\underline{e}_3\underline{e}_1 + 0 + QT_{33,i}\underline{e}_3\underline{e}_3$$

$QT(3,1,2)=-1$

$QT(2,2,3)=1$

$QT(1,3,4)=-1$

$QT(3,3,5)=1$

$QT(1,1,6)=X$

$QT(3,1,6)=-Z$

$QT(3,1,7)=-X$

$QT(2,2,8)=X$

$QT(1,3,9)=-X$

$QT(3,3,9)=Z$

$QT(3,3,1)=X$

```
QT(1,1,11)=Z

QT(1,3,12)=-Z

QT(2,2,13)=Z
```

3x3 Gauss Quadrature on this Element.

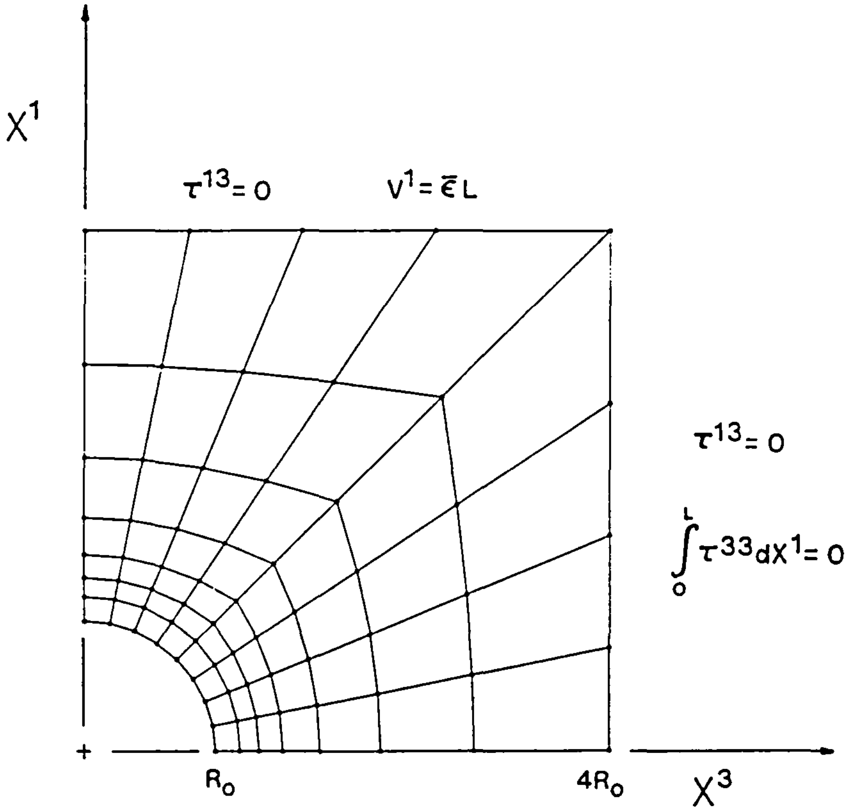

Figure 1. Finite Element Mesh and Boundary Conditions for the Problem of Growth of a Void.

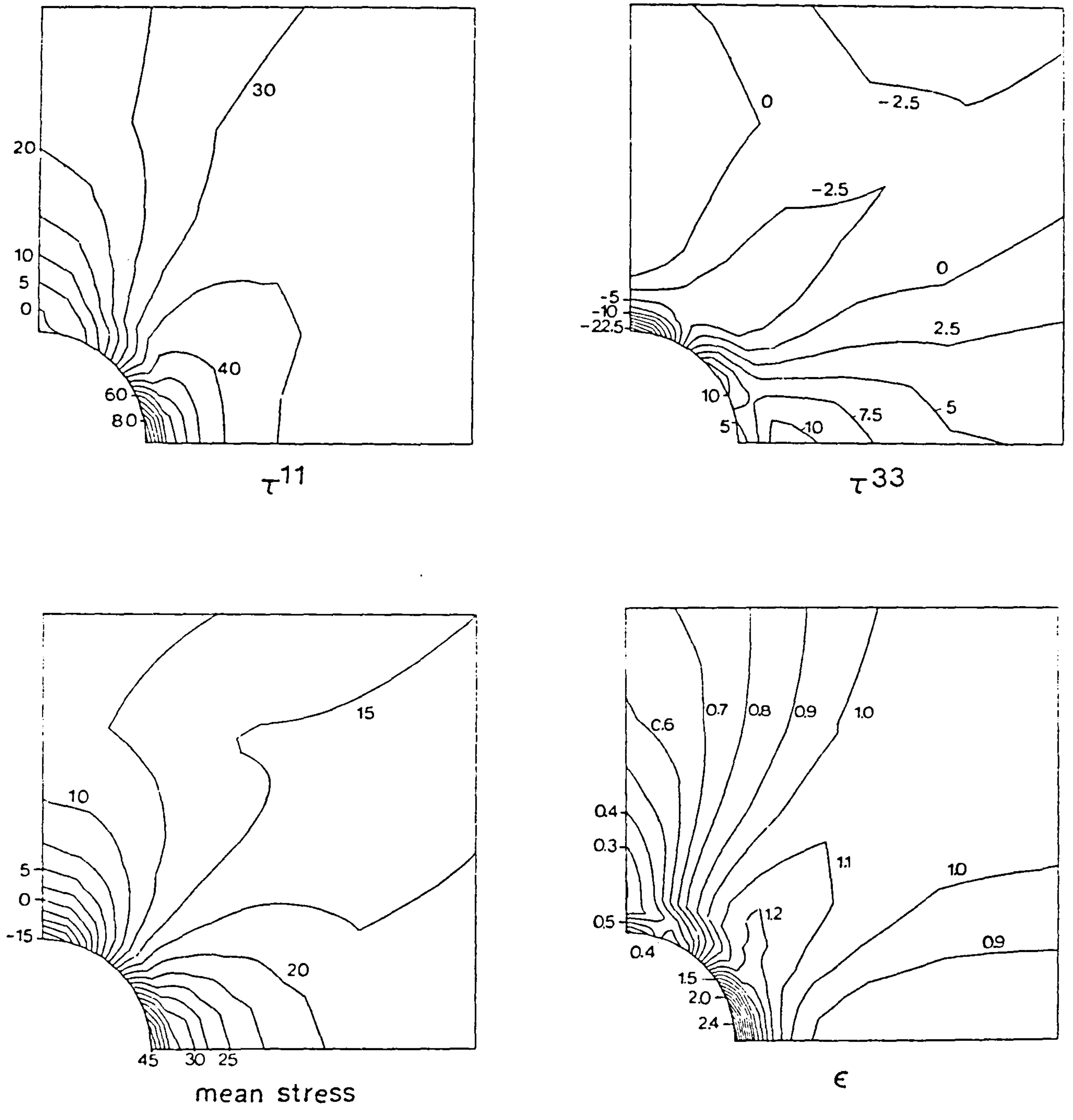
τ^{11} τ^{33} mean stress ϵ

Figure 2-5. Stresses and Mean Strain Rate at Elongation Ratio L=1.01.

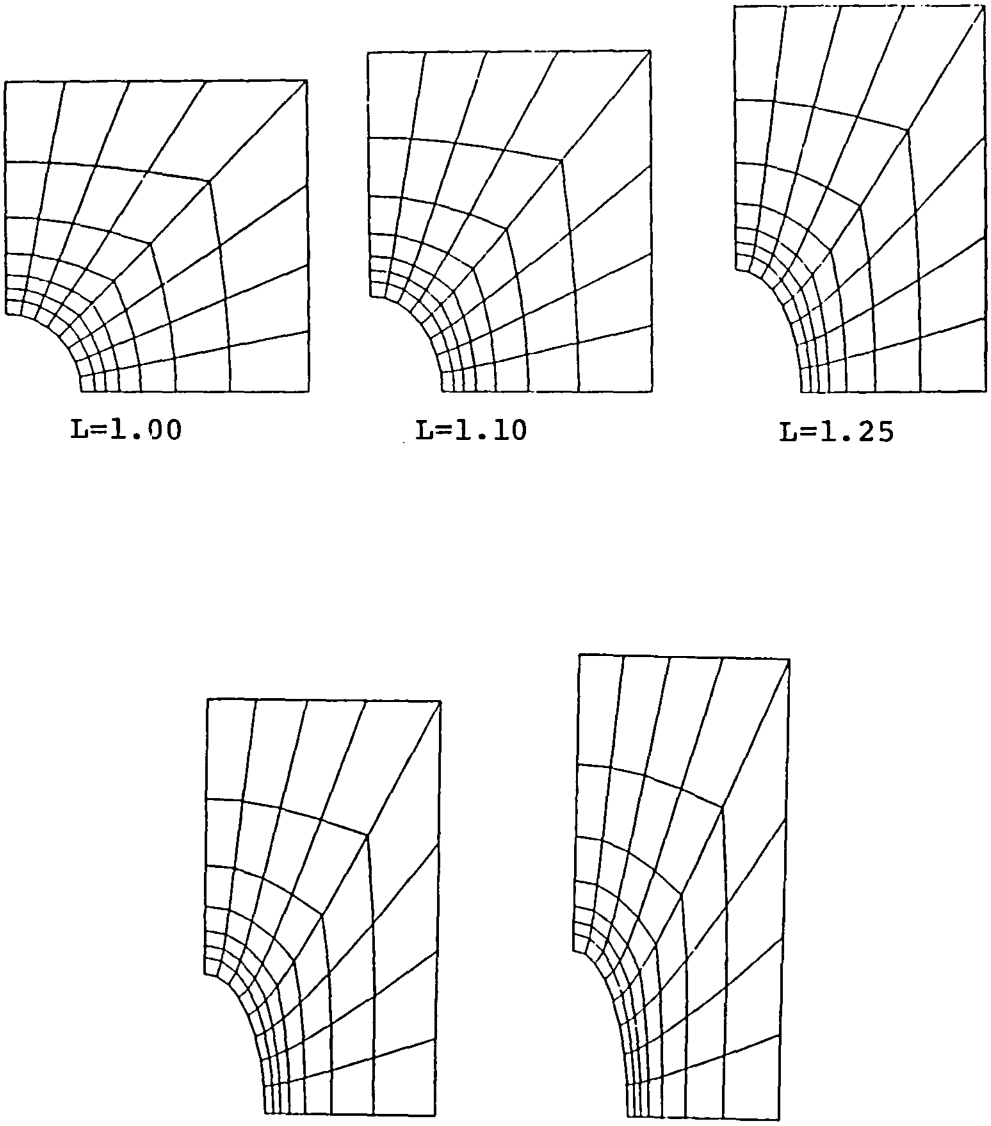

L=1.00 L=1.10 L=1.25

L=1.35 L=1.50

Figure 6. Deformation of Cell.

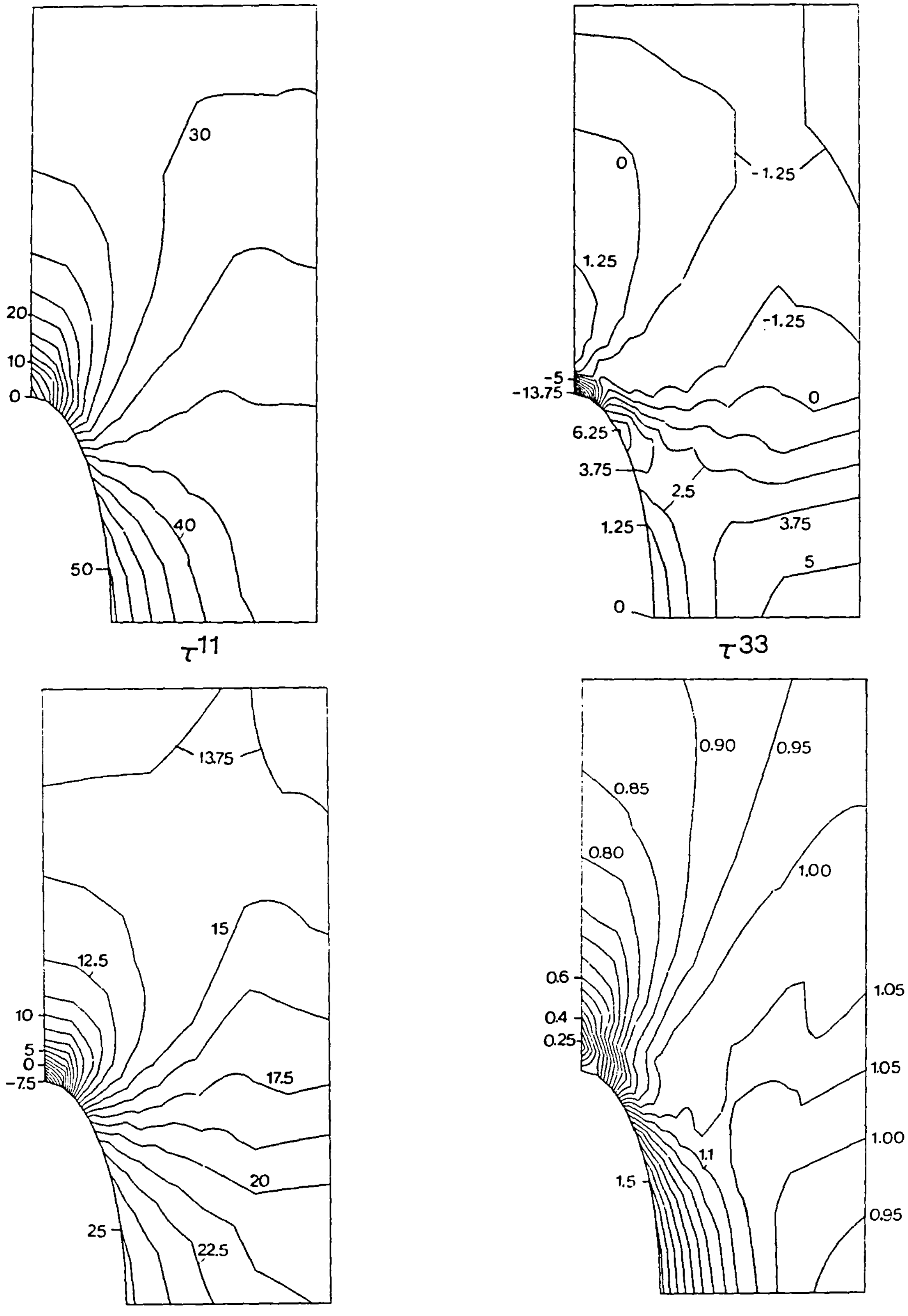

τ^{11} τ^{33}

mean stress ϵ

Figure 7-10. Stresses and Mean Strain at Elongation Ratio L=1.50.

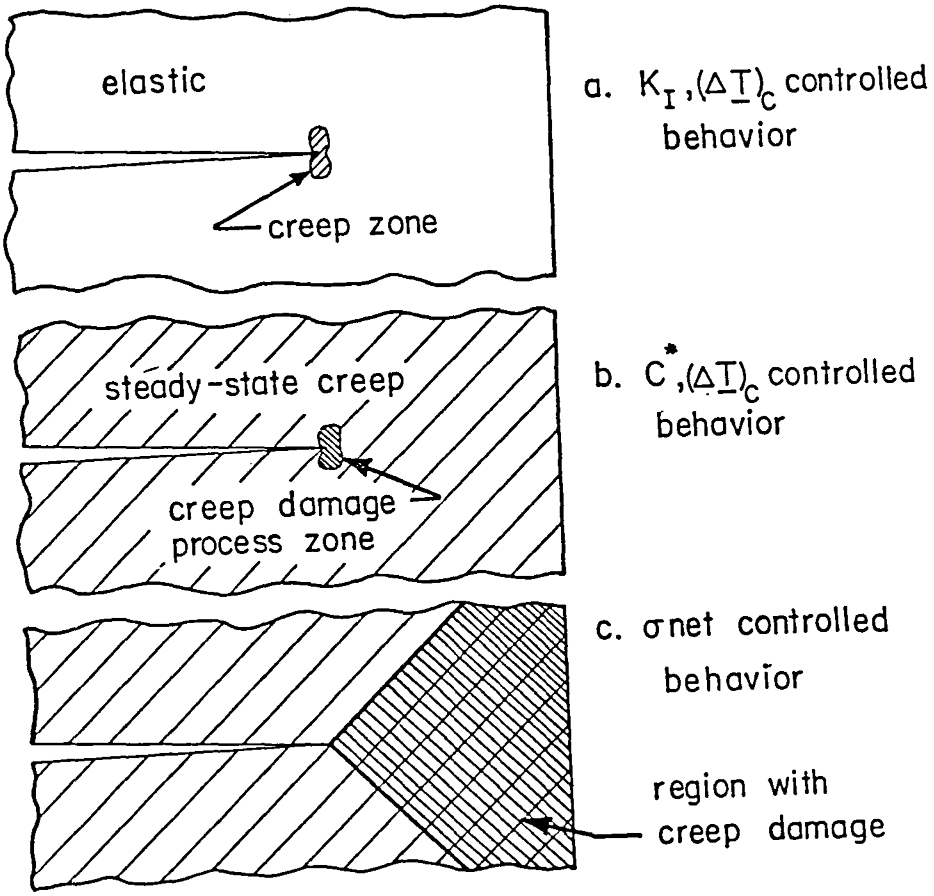

Figure 11. Conditions for which Creep Crack Growth Parameters are Expected to be Valid.

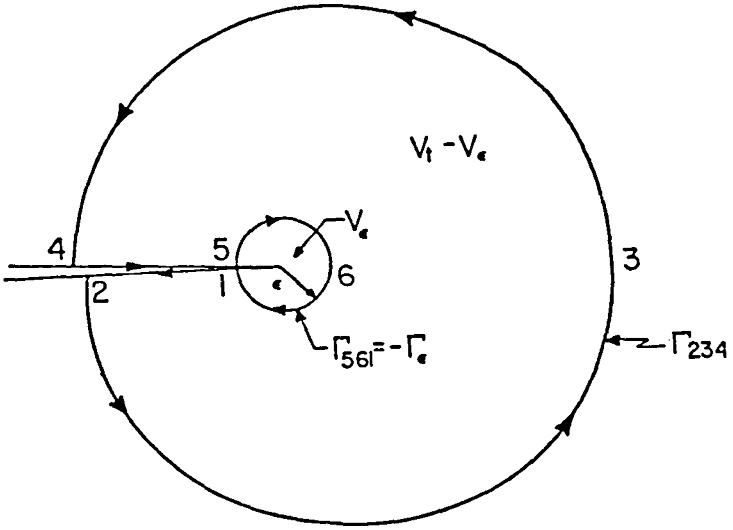

Figure 12. Contours for Applying the Conservation Law to a Two-Dimensional, Cracked Body.

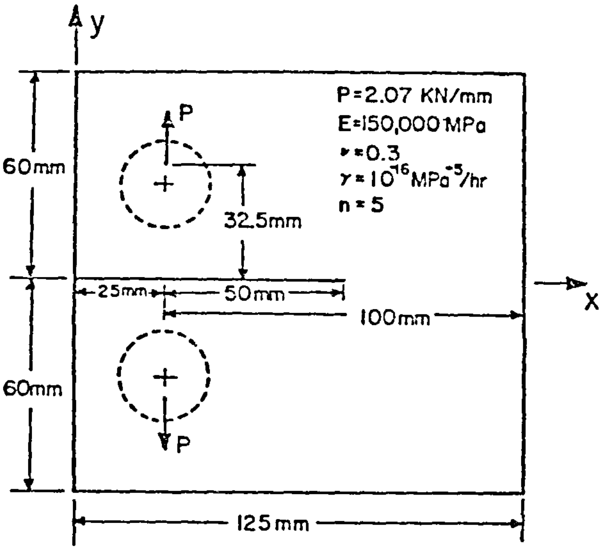

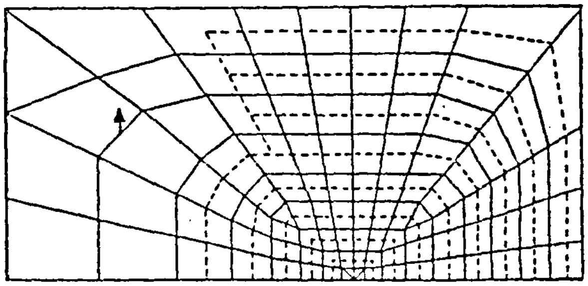

The 102 element mesh (331 nodes; 642 d.o.f.)

The 300 element mesh (941 nodes; 1840 d.o.f)

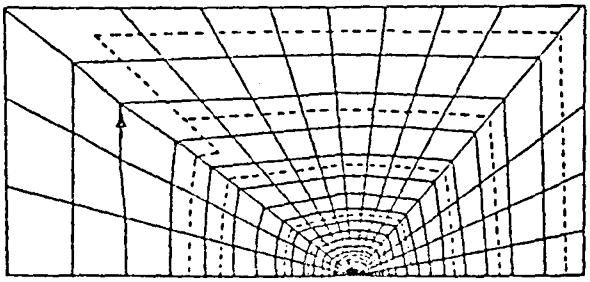

Figure 13. Summary of Geometry, Loading, Material Properties and Finite Element Meshes for the Compact Specimen.

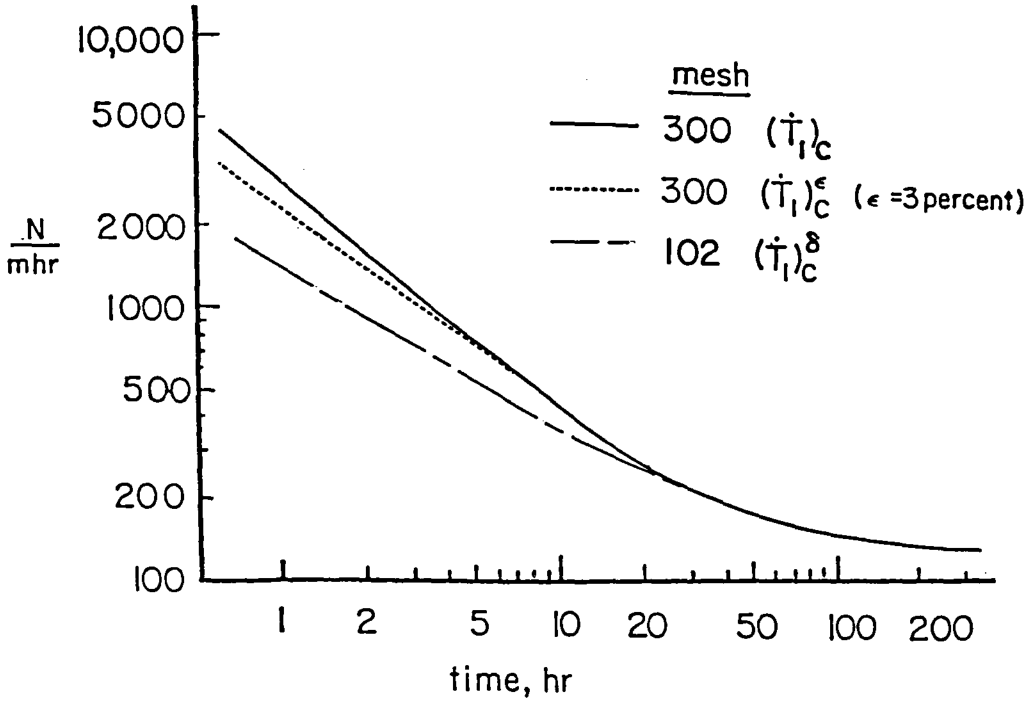

Figure 14. Comparison of $(\dot{T}_1)_c$ and $(\dot{T}_1)_c^\delta$ for the compact specimen.

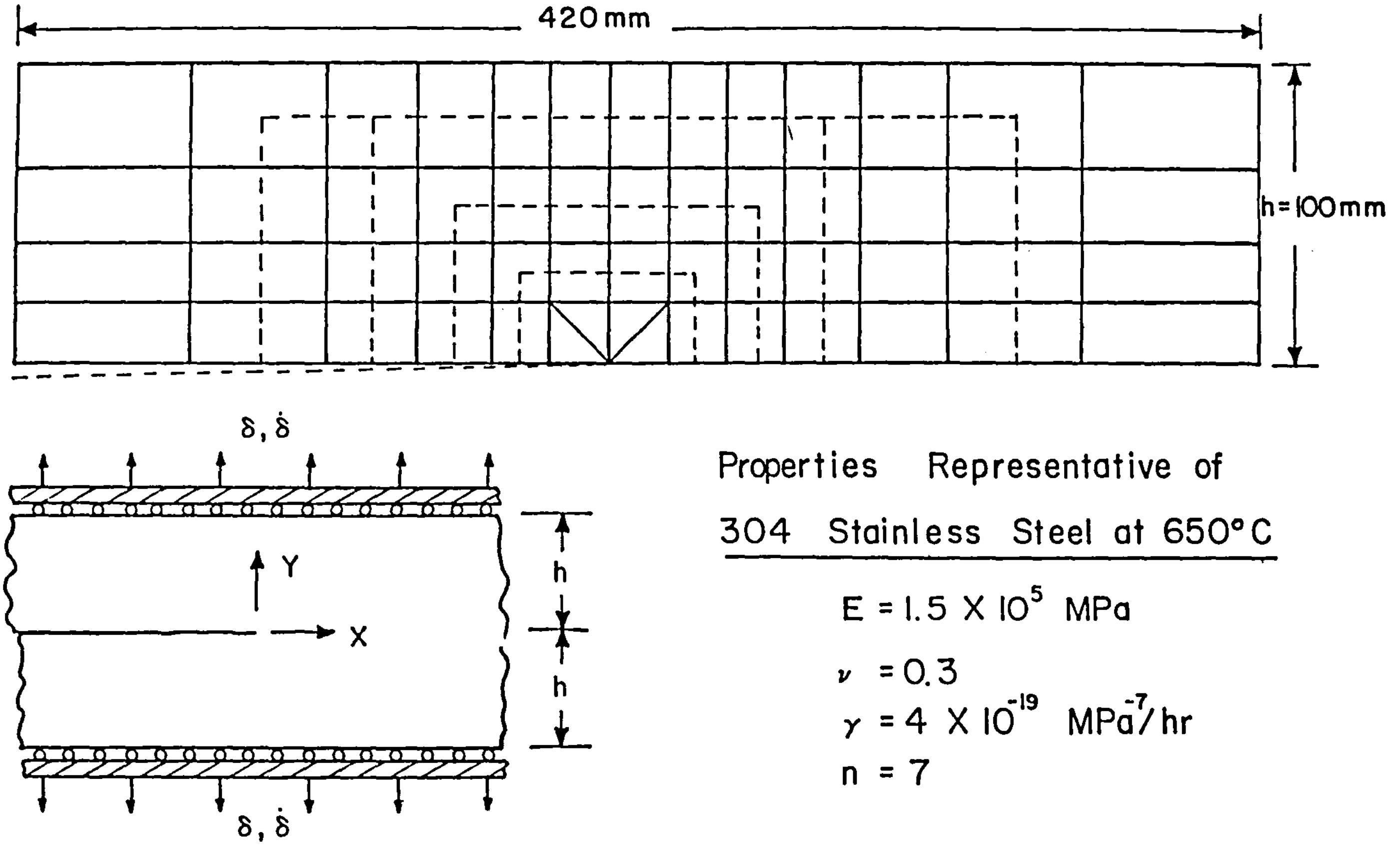

Figure 15. Summary of Geometry, Loading, Material Properties and Finite Element Meshes for the Compact Specimen.

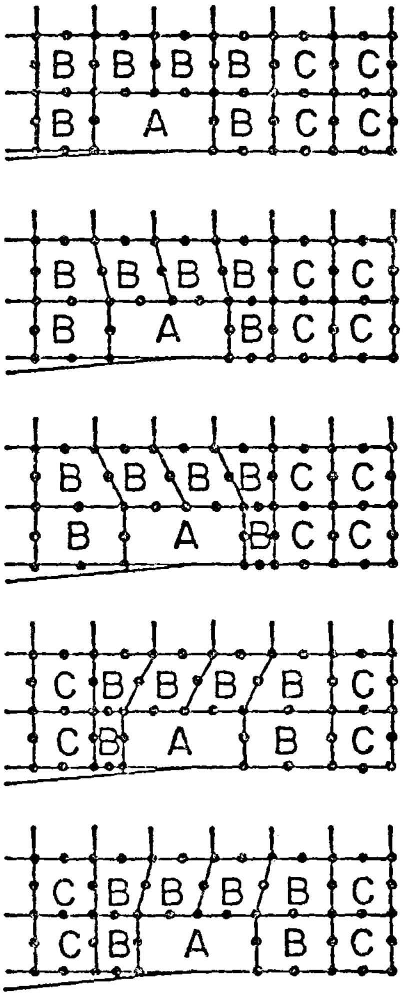

Figure 16. Illustration of Mesh Shifting/Remeshing Procedure for Simulation of Crack Growth.

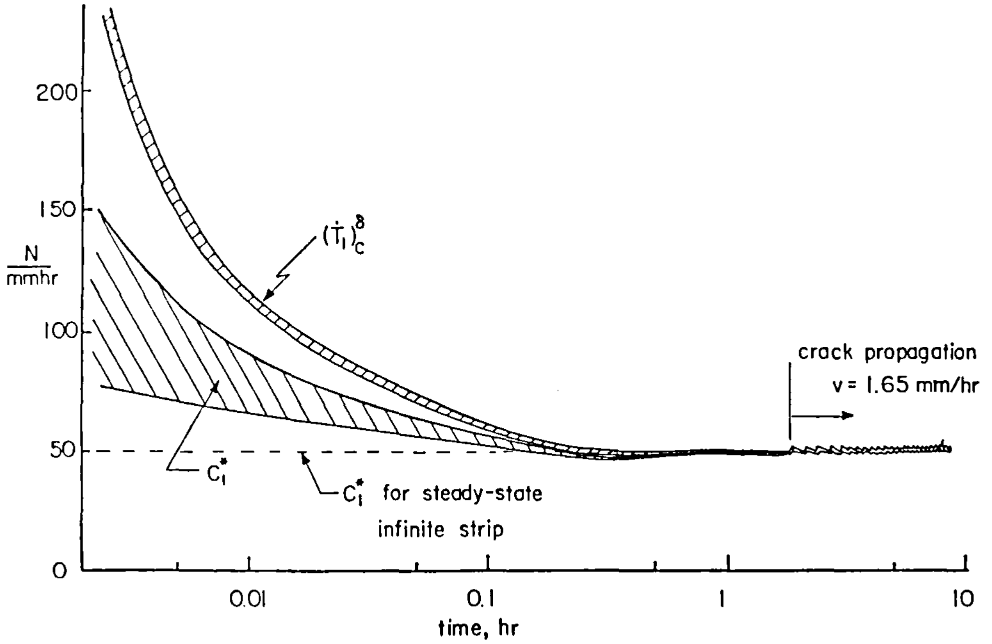

Figure 17. History of $(\dot{T}_1)_c^\delta$ and C_1^* for Creep Crack Growth in a Plane Strip (Steady-State C_1^*=50 N/mm.hr, da/dt=1.65 mm/hr).

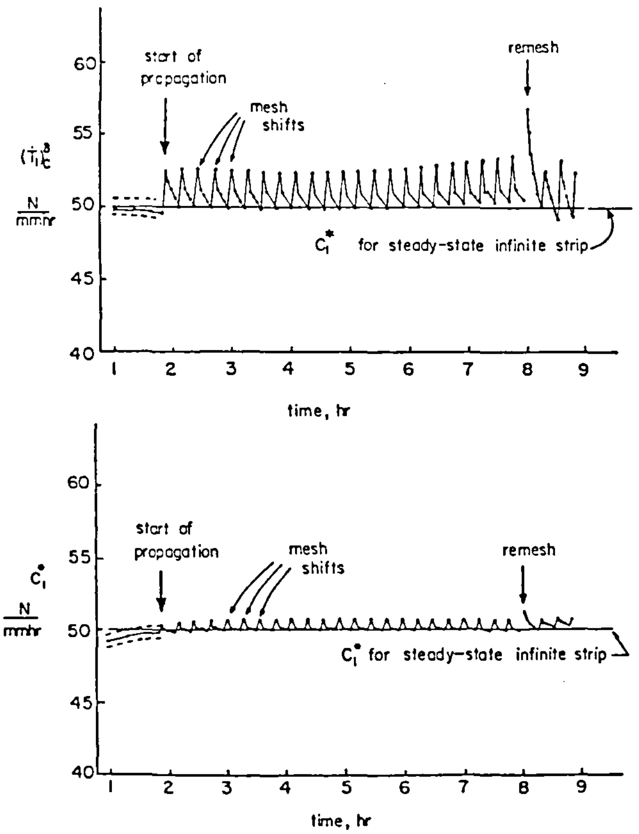

Figure 18. Behavior of $(\dot{T}_1)_c^\delta$ and C_1^* During Simulated Creep Crack Growth in a Plane-Strain Strip (Steady-State C_1^*=50 N/mm.hr da/dt=0.11 mm/hr).

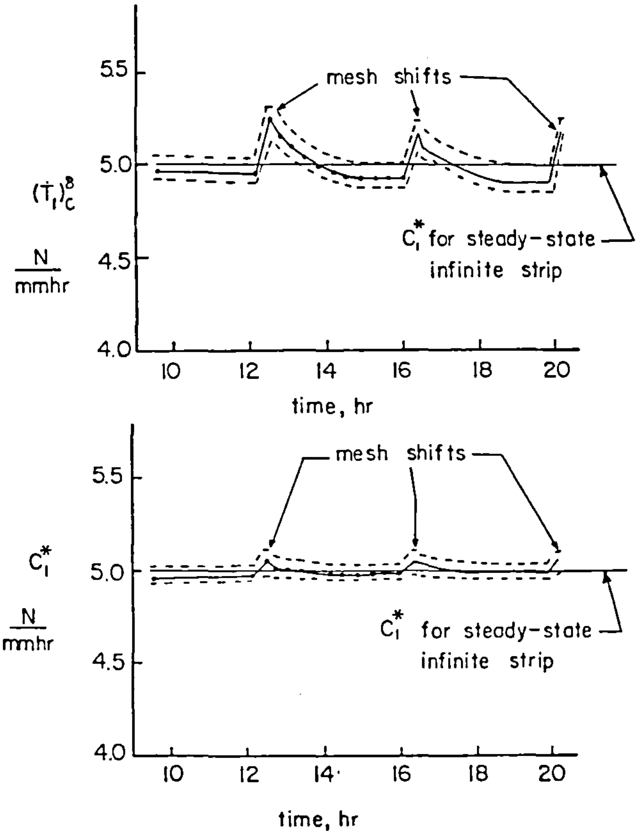

Figure 19. (Behavior of $(\dot{T}_1)_c^\delta$ and During Simulated Creep Crack Growth in a Plane Strain Stip (Steady-State C_1^*=5 N/mm.hr, da/dt=0.111 mm/hr).

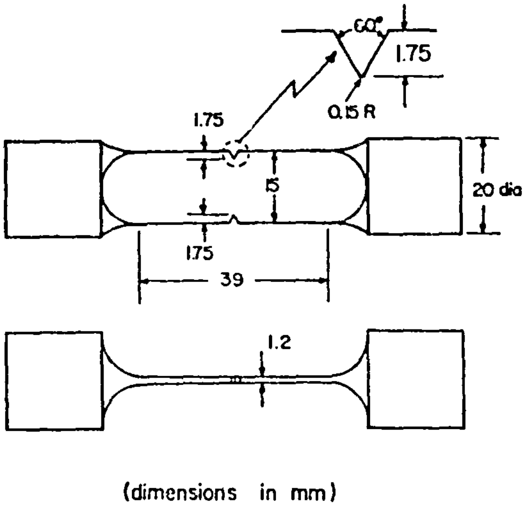

Figure 20. Geometry of Double-Edge Crack Specimen.

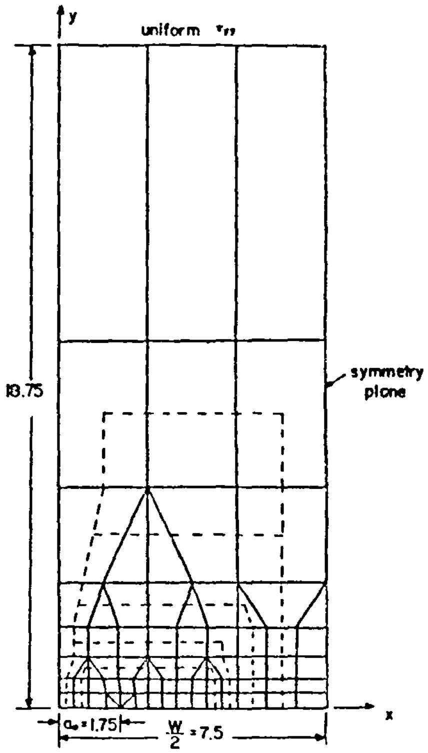

Figure. 21. Finite Element Model and ($\hat{T}$) Integral Path for the DEC Specimen.

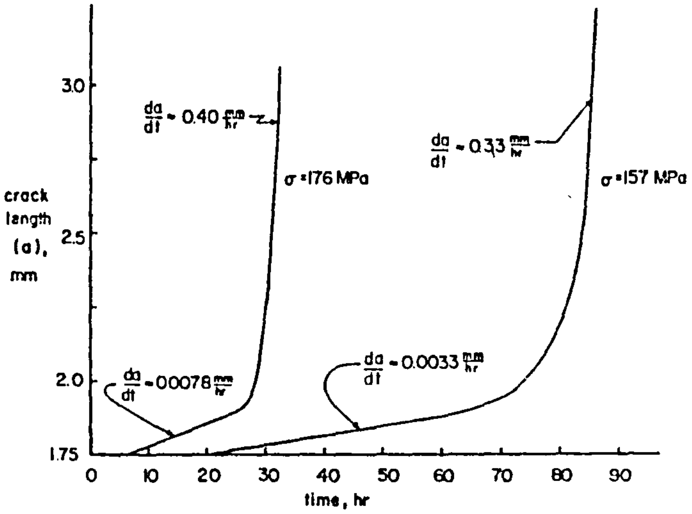

Figure 22. Experimentally Determined Crack Growth Histories (From Koterazawa and Iwata).

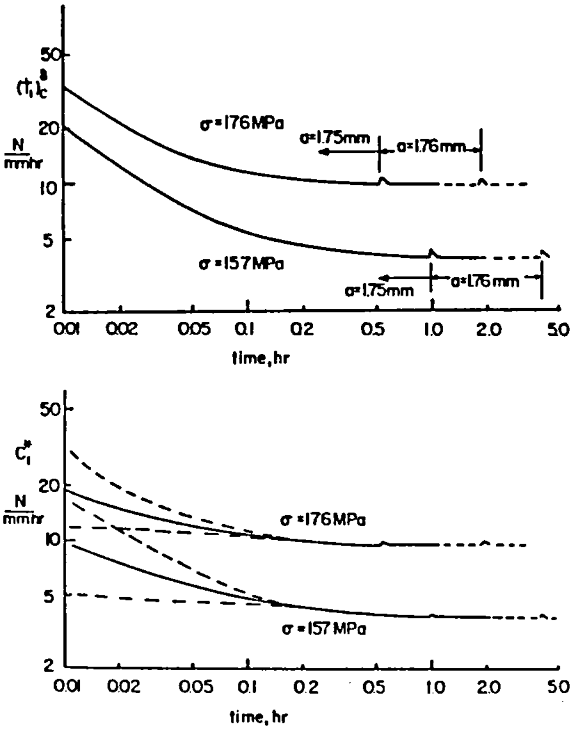

Figure. 23. Values of ($\dot{T}$) and C* During Earlier Phases of Creep Crack Growth.

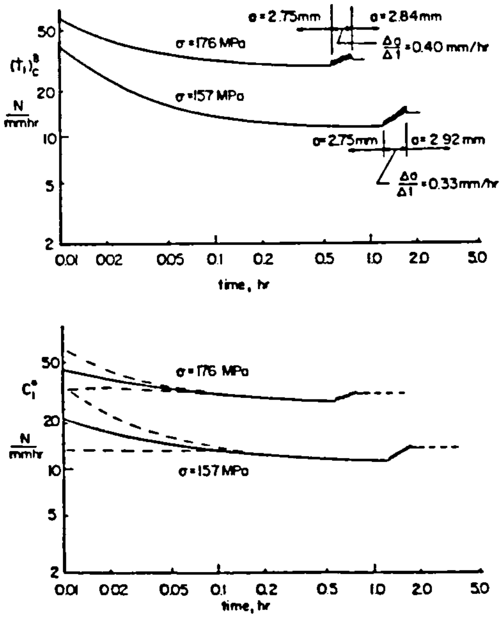

Figure 24. Values of ($\dot{T}$) and C* During Latter Phases of Creep Crack Growth.